

# Scaling effects of rigid kite ground-generation airborne wind energy systems

Markus Sommerfeld<sup>1</sup>, Martin Dörenkämper<sup>2</sup>, Jochem De Schutter<sup>3</sup>, and Curran Crawford<sup>1</sup>

<sup>1</sup>Institute for Integrated Energy Systems, University of Victoria, British Columbia, Canada

<sup>2</sup>Fraunhofer Institute for Wind Energy Systems, Oldenburg, Germany

<sup>3</sup>Systems Control and Optimization Laboratory IMTEK, Freiburg, Germany

**Correspondence:** Markus Sommerfeld (msommerf@uvic.ca)

**Abstract.** While some Airborne Wind Energy System (AWES) companies aim at small, temporary or remote off-grid markets, others aim at utility-scale, multi-megawatt integration into the electricity grid. This study investigates the scaling effects of single-wing, ground-generation Airborne Wind Energy Systems from small to utility-scale systems, subject to realistic 10-minute, onshore and offshore wind conditions derived from the numerical mesoscale weather research and forecasting (WRF) model. To reduce computational cost, wind velocity profiles are grouped into  $k = 10$  clusters using k-means clustering. Three representative profiles from each cluster are implemented into an AWES nonlinear optimal control model, to determine power-optimal trajectories. We compare the effects of three different aircraft masses and two sets of nonlinear aerodynamic coefficients for each aircraft, with wing areas ranging from  $10 \text{ m}^2$  to  $150 \text{ m}^2$ , on operating [heights parameters](#) and trajectories. We predict size- and weight-dependent AWES power curves, annual energy production (AEP) and capacity factor (cf) [and compare them to a quasi-steady state reference model](#). ~~Tether impacts, such as~~ [Instantaneous force, tether speed and power fluctuations as well as](#) power losses associated with tether drag and ~~the tether contribution to total~~ system mass are quantified.

[Instantaneous force, tether speed and power fluctuations as well as](#) power losses associated with tether drag and ~~the tether contribution to total~~ system mass are quantified. ~~Furthermore, we estimate a minimum average cycle-average lift-to-weight ratio, above which ground-generation AWES can operate, to explore the viable AWES mass budget.~~

## 15 1 Introduction

Airborne wind energy systems (AWESs) harvest wind energy from the stronger and less turbulent winds at mid-altitude, here defined as heights above 100 m and below 1500 m. These beneficial conditions promise more reliable and stable wind power generation compared to the conventional wind turbines (WTs) at lower altitudes. The light, tower-less design allows for mobile deployment and reduces the capital cost of AWESs (Lunney et al., 2017). These kite inspired systems consist of ~~an~~ one or more autonomous aircraft which ~~is~~ are connected to a ground station via one or more tethers. While various designs are investigated, two major crosswind concepts are currently considered by industry: the ground-generation also referred to as pumping-mode, and on-board-generation also referred to as drag-mode. This study focuses on the two-phase, ground-generation concept, as it is currently the main concept pursued by industry ~~. after Makani Technologies LLC (Makani, 2020), the biggest company and proponent of the on-board-generation concept closed in February 2020.~~ On-board-generation AWES carry additional weight with the on-board generator and propeller mass, as well as the heavier, conductive tether. ~~Part of the reason for the closure could have been that the company did not see a viable road to commercialization. Thus a motivation to have a closer look at ground-gen scaling. One of the biggest companies working on this concept is Ampyx Power (Ampyx, 2020).~~ Ground-generation AWES generate power during the reel-out phase while the wing generates large lift forces and pulls the tether from a drum. During the following reel-in phase a fraction of the energy is consumed to return the aircraft back to its initial position and restart the cycle (Luchsinger, 2013). As a result, the power generated by such systems is inherently oscillating which could be offset using multiple devices in a wind farm setup or buffering the energy before feeding it into the grid (Malz et al., 2018).

Over the last years, two main AWES applications emerged. The first makes use of the mobile nature of the technology which allows the deployment in inaccessible or remote places such as temporary mines or remote off-grid communities as these locations often rely on expensive diesel generators. Second is the grid-scale integration of AWES, which requires up-scaling the systems to compete with fossil and renewable energy sources in the energy market. One example is Ampyx Power (Ampyx, 2020) which aims to re-power decommissioned offshore wind farms or deploy floating platforms added citation (offshorewind.biz), expecting higher energy yield due to better wind conditions, which in combination with design choices lead to lower levelized cost of electricity. Additionally, setting up AWES offshore allows for safer operation and is likely to be socially more accepted (Ellis and Ferraro, 2016).

Determining realistic performance of AWES is difficult as AWES trajectory depends on many variables that are not represented in simple models. Wind velocity profiles, aerodynamic coefficients, tether drag, aircraft mass and AWES size impact AWES trajectory and therefore generated power. Using an optimization algorithm it is possible to implement these variables and determine optimal AWES performance.

We therefore investigate the scalability and design space of small to large-scale AWES, both offshore and onshore. Depending on the aircraft wing surface area, aerodynamic coefficients and the tether diameter, rated power ranges from  $\bar{P}_{\text{rated}} = 145 \text{ kW}$  to  $199 \text{ kW}$  for  $A_{\text{wing}} = 10 \text{ m}^2$  and  $\bar{P}_{\text{rated}} = 2010 \text{ kW}$  to  $3430 \text{ kW}$ . We compare the optimal system performance subject to various wing mass for representative onshore and offshore wind conditions.

In comparison to the commonly used logarithmic wind speed profile, this WRF-derived set of wind data includes the wind direction rotation with height and the complex range of profile shapes emerging from atmospheric stability. This includes almost constant wind velocity profiles associated with unsteady stratification, high shear wind velocity profiles resulting from stable conditions, as well as non-monotonic wind velocity profiles including low level jets (LLJs). The power output of an AWES not only depends on the wing size, but also the prevalent wind velocity profile shape and magnitude which result in distinct trajectories and operating altitudes. Therefore, a representative wind data set up to mid-altitudes, here defined as heights above 100 m and below 1500 m, is necessary to determine realistic AWES performance. This study relies on mesoscale numerical weather prediction models such as the Weather Research and Forecasting (WRF) model, which is well known for conventional WT siting applications (Salvação and Guedes Soares, 2018; Dörenkämper et al., 2020), as measuring wind conditions at mid-altitudes is difficult due to reduced data availability aloft (Sommerfeld et al., 2019a). To reduce the computational cost, 10-minute average wind speed profiles were clustered using the k-means clustering method described in (Sommerfeld, 2020). We compare AWES performance for an onshore location in northern Germany near Pritzwalk (Sommerfeld et al., 2019b) and an offshore location at the FINO3 research platform in the North Sea. These wind clustered wind conditions were implemented into the `awebox` (awebox, 2020) optimization framework which computes periodic flight trajectories that maximize average mechanical power output.

In comparison to our previous studies, which derived onshore and offshore AWES power curves, this paper explores the AWES design space from small to to utility-scale. We aim at setting up-scaling design and mass targets, instead of a detailed system design. While other studies rely on simplified logarithmic wind speed profiles De Schutter et al. (2019) , [high resolution Large eddy simulation \(LES\)](#) Haas et al. (2019) or reanalysis data sets [added](#) Schelbergen et al. (2020) [to investigate general behavior, performance, trajectory or wake effects](#), we optimize AWES trajectory subject to realistic 10 minute mesoscale wind data, which allows better optimal performance prediction. ~~This support decision-making regarding location-specific design, power estimation and scaling limitations.~~

[The main contribution is the presentation of scaling effects on ground-station AWES subject to realistic wind velocity profiles. The here described results inform decision-making regarding location-specific design, power estimation and scaling limitations.](#)

Section 2 summarizes the onshore and offshore wind resource as well as the clustering results. For a detailed description of the WRF model and clustering algorithm see (Sommerfeld, 2020). Section 3 briefly introduces the AWES model and optimization method as well as the implemented constraints and initialization. Section 4 compares the results for six AWES sizes with three different mass scaling assumptions and two sets of non-linear aerodynamic coefficients. We present, inter alia, trajectories, power curves and annual energy production estimates for a representative onshore and offshore location. Finally, Section 5 concludes the article with an outlook and motivation for future work to continue to advance AWES towards commercial reality.

This study considers representative 10 min onshore (northern Germany, lat:  $53^{\circ}10'47.00''\text{N}$ , lon:  $12^{\circ}11'20.98''\text{E}$ ) and offshore wind data (FINO3 research platform, lat:  $55^{\circ}11,7'\text{N}$ , lon:  $7^{\circ}9,5'\text{E}$ ) derived from 12 months of WRF simulations each. Both locations are highlighted by a black dot in figure 1.

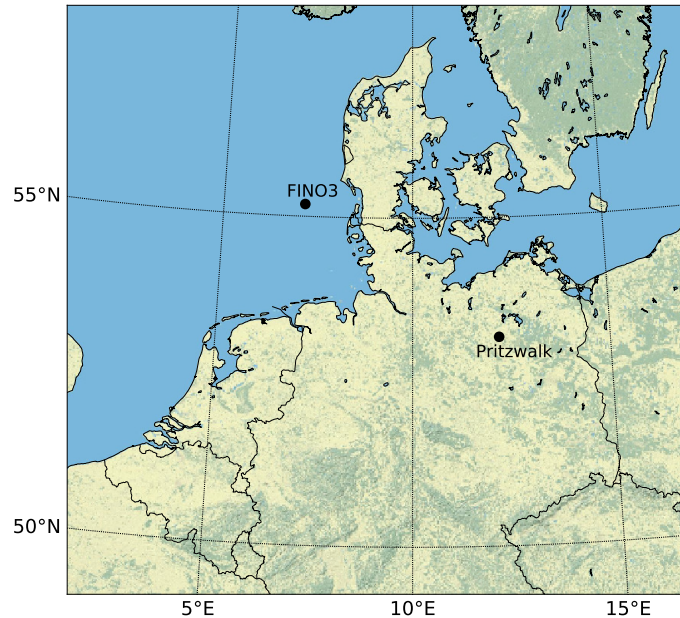


**Figure 1.** Topography map of northern Germany with the representative onshore (Pritzwalk) and offshore (FINO3) locations highlighted with a black dot.

Both horizontal velocity components of the resulting mesoscale wind data set are clustered using a k-means clustering  
 85 algorithm (Pedregosa et al., 2011). According to previous investigations (Sommerfeld, 2020), a small number of clusters with few representative profiles per cluster yield good power and AEP estimates at reasonable computational cost. Therefore, the wind velocity profiles were grouped into  $k = 10$  clusters from which the 5th, 50th and 95th percentile (sorted by wind speed at 200 m) were implemented into the optimization algorithm as design points to cover the entire annual wind regime.

The resulting average wind velocity profiles for each of the ten clusters, also known as centroids, are shown in the top  
 90 row of figure 2. For presentation purposes, only each centroid's wind speed magnitude, colored according to average wind speed up to 500 m, is shown. The complete set of clustered profiles profiles are shown in grey. The cluster average wind profile shapes show wind shears typically associated with unstable and stable conditions. They follow expected location-specific trends

with lower wind shear and higher wind speeds offshore (right) in comparison to onshore (left). The associated, color-coded annual centroid frequency is shown in the center. The bottom subfigures summarize the wind speed probability distribution at a reference height of  $100 \leq z \leq 400$  m. We chose this reference height as a proxy for wind speed at operating altitude, because an a priori estimation is impossible, and onshore and offshore power curves are almost identical using this reference wind speed. For a detailed description of the WRF model and setup, the clustering process as well as the correlation between clusters and stability conditions see (Sommerfeld, 2020).

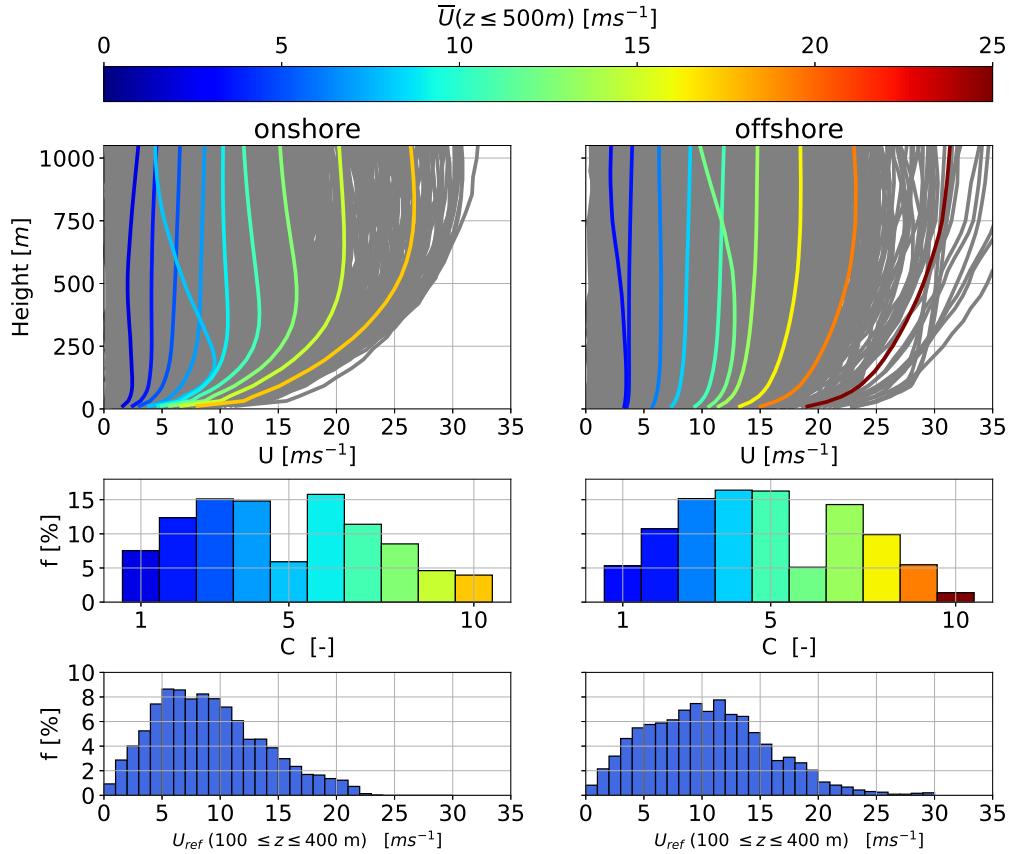


**Figure 2.** Onshore (left) and offshore (right) annual cluster average wind speed profiles (centroids) resulting from the k-means clustering process for  $k = 10$  (top). Underlying WRF simulated wind speed profiles depicted in grey. The centroids are sorted, labeled and colored in according to average wind speed up to 500 m. The corresponding cluster frequency  $f$  for each cluster  $C$  is shown in the center. The bottom figures show the wind speed probability distribution at a reference height of  $100 \leq z \leq 400$  m.

### 3 AWES trajectory optimization model

100 ~~The investigation of the scaling potential of AWESs~~ [Investigating the AWES scaling potential](#) not only requires understanding of wind conditions at higher altitudes, but also of AWES power production, which is intrinsically linked to the aircraft's flight dynamics, as the AWES never reaches a steady state over the course of a power cycle. Hence power output estimation based on steady-state simplifications [only give a rough estimate, but can not describe the variation of system parameters or operating trajectory which determine power production. particularly for realistic, non-monotonic wind profiles.](#) ~~are generally not suited~~  
105 ~~for describing the effects of realistic wind profiles or varying system parameters on the power output over the entire operational window.~~ Therefore we make use of optimal control methods to compute power-optimal, dynamically feasible flight trajectories that satisfy operation constraints such as flight envelope and structural system limits. [We compare the optimization results to a simplified quasi steady-state \(QSS\) engineering AWES model \(sub-section 3.2 to verify our results and to highlight the difference between both models.](#)

#### 110 3.1 Model overview

We compute ground-generation AWES power cycles by solving a periodic optimal control problem which maximizes the cycle-average AWES power output  $\bar{P}$ . In periodic optimal control, the system state at the initial and final time of the trajectory must be equal, but are chosen freely by the optimizer. This methodology, implemented in the open-source software framework `awebox` (awebox, 2020), is used to generate power-optimal trajectories for single-wing ground-generation AWES sizes with  
115 various wing area, mass and aerodynamic performance. Table 2 summarizes the imposed constraints for each system design.

The AWES model considers a 6 degree of freedom (DOF) rigid-wing aircraft model with pre-computed quadratic lift, drag and pitch moment coefficients, which is controlled via aileron, elevator and rudder deflection rates. For this scaling study, the Ampyx AP2 reference model (Ampyx, 2020; Malz et al., 2019) serves as a base from which the aircraft size and mass as well as aerodynamic coefficients were scaled (see sections 3.4 and 3.6).

120 While the ground station dynamics are not explicitly modeled, constraints on tether speed, acceleration and jerk are implemented to ensure a realistic operating envelope. For this study a reel-out to reel-in ratio of  $\frac{2}{3}$  ( $\frac{v_{out}}{v_{in}} = \frac{10 \text{ ms}^{-1}}{15 \text{ ms}^{-1}}$ ) was chosen. Tether acceleration  $\ddot{l}_{max} = 10 \text{ ms}^{-2}$  and tether jerk  $\dddot{l}_{max} = 100 \text{ ms}^{-3}$  were limited to simulate generator torque constraints. [Tether tension is defined by its diameter and maximum strain. The tether diameter has been chosen such that maximum average cycle power is achieved at an approximate wind speed of 10 ms.](#)

125 For a more detailed description of the model and the optimization algorithm see (Sommerfeld, 2020; Leuthold et al., 2018; De Schutter et al., 2019; Bronnenmeyer, 2018; Horn et al., 2013; Haas et al., 2019).

#### 3.2 [Quasi-steady state reference model](#)

To contextualize the optimization results, a quasi-steady state model (QSS) based on Loyd's crosswind approximation Loyd (1980) is introduced. This model has been adapted by Schmehl et al. Schmehl et al. (2013) to include misalignment losses.  
130 [It neglects aircraft and tether mass and assumes a quasi-steady state with the wing moving directly cross-wind with zero](#)

azimuth angle  $\phi = 0$  relative to the wind direction. Tether speed  $v_t$  is non-dimensionalized as the reeling factor ( $f = \frac{v_t}{U}$ ) with an optimal value of  $f_{\text{opt}} = \frac{1}{3} \cos \theta \cos \phi$ . Equation 1 estimates optimal power  $P_{\text{opt}}$  as a function of wind speed  $U$  at altitude  $z$  and the resultant aerodynamic force coefficient  $c_R$  (see equation 2), which is calculated from the aerodynamic lift  $c_L$  and total drag coefficient  $c_{D,\text{total}}$ . Tether drag is included in the total AWES drag coefficient  $c_{D,\text{total}}$  according to a simplified estimation  
 135 3 Houska and Diehl (2007); Argatov and Silvennoinen (2013); van der Vlugt et al. (2019); Schmehl et al. (2013). Maximizing  $c_R^3/c_{D,\text{total}}^2$  in turn maximizes  $P_{\text{opt}}$ . A linear approximation of the standard atmosphere yields air density  $\rho_{\text{air}}(z)$  at altitude  $z$  Champion et al. (1985) ( $\rho_{\text{air}}(z) = 1.225 \text{ kgm}^{-3} - 0.00011 \text{ kgm}^{-4}z$ ). Elevation angle  $\theta = \arcsin(\frac{z}{l_{\text{tether}}})$  is derived from altitude  $z$  and tether length  $l_{\text{tether}}$ .

$$P_{\text{opt}} = \frac{\rho_{\text{air}}(z)}{2} U(z)^3 c_R \left( \frac{c_R}{c_{D,\text{total}}} \right)^2 f_{\text{opt}} (\cos \theta \cos \phi - f_{\text{opt}})^2 \quad (1)$$

$$140 \quad c_R = \sqrt{c_L^2 + c_{D,\text{total}}^2} \quad (2)$$

The total drag coefficient  $c_{D,\text{total}}$  determines the air resistance of the entire AWES in crosswind motion. It highly depends on the tether diameter  $d_{\text{tether}}$  and length  $l_{\text{tether}}$ , as well as the wing area  $A_{\text{wing}}$ . The aerodynamic drag coefficient of the wing  $c_{D,\text{wing}}$  is defined by the wing shape. We consider a cylindrical tether with constant diameter and an aerodynamic tether drag coefficient  $c_{D,\text{tether}}$  of 1.0. The tether drag coefficient could even be higher for braided tethers. For the sake of simplicity, tether  
 145 slope is not considered in the drag calculation, which leads to an over estimation of tether drag. A more accurate tether model would further include the wind speed variation with height. Assuming a uniform wind, the line integral along the tether results in a total effective drag coefficient of Houska and Diehl (2007); Argatov and Silvennoinen (2013); van der Vlugt et al. (2019):

$$c_{D,\text{total}} = c_{D,\text{wing}} + \frac{1}{4} \frac{d_{\text{tether}} l_{\text{tether}}}{A_{\text{wing}}} c_{D,\text{tether}} \quad (3)$$

Both the QSS and optimization model are subject to the same constraints (table 2). Optimal power of the QSS model is  
 150 estimated by varying tether length up to 2000 m for every given wind profile (section 3.3) and applying the above described tether drag and elevation losses. A minimal operating altitude is enforced. The QSS-predicted power used for reference in section 4.5 is the highest power for a given wind profile. Therefore, optimal operating height is the height at which the highest power is calculated.

### 3.3 Wind profile implementation

155 The 2D horizontal wind velocity profiles were clustered into  $k = 10$  clusters. Three representative profiles from each cluster as well as each cluster's centroid, rotated such that the main wind direction  $u$  points in positive  $x$  direction and the deviation  $v$  from it points in positive  $y$  direction, were implemented. This assumes omnidirectional AWES operation, which simplifies the comparison of results. We interpolate the  $u$  and  $v$  components using Lagrange polynomials to obtain a twice continuously

differentiable function representation of the wind velocity profiles, which is necessary formulate an optimal control problem  
 160 that can be solved with the gradient-based nonlinear programming (NLP) solver IPOPT (noa, 2016).

### 3.4 System Aircraft scaling

Aircraft mass  $m$  and inertia  $\mathbf{J}$  are scaled relative to the Ampyx AP2 reference model (Malz et al., 2019; Ampyx, 2020) according to simplified geometric scaling laws relative to wing span  $b$  (see equation (4)). The mass scaling exponent  $\kappa$  ranges from 2.7 to 3.3. An exponent of 3 represents pure geometric scaling, while  $\kappa = 2.7$  implies positive scaling effects and weight  
 165 savings with size, while  $\kappa = 3.3$  assumes negative scaling. ~~Based on the wing area, maximum tether force and diameter are scaled while tether speed and acceleration constraints are kept constant.~~ [A review of available literature shows that anticipated AWES scaling exponents vary between  \$\kappa = 2.2 - 2.6\$  \(grey area\), shown in 3. We assume more conservative mass scaling for the purpose of this investigation.](#)

Makani’s openly published technical reports describe their “M600 SN6” as well as their MX2 (*Oktoberkite*) design, which  
 170 redesigned the M600 airframe to overcome some of its shortcomings and produce  $\bar{P}_{MX2} = 600\text{kW}$  at a wind speed of  $U_{MX2\text{-ref}} = 11\text{ms}^{-1}$  at operating height (Echeverri et al., 2020). Note that Makani’s on-board-generation concept is inherently heavier than the ground-generation concept considered here, because of propellers, generators and supporting structures. The intended M600 design specified a mass of 919 kg, which corresponds to an AP2 mass scaling exponent of  $\kappa = 2.72$ . The as-built M600 had a wing area of  $A_{\text{wing}} = 32.9\text{m}^2$  and a mass  $m_{M600} = 1730.8\text{kg}$ . If we scale the AP2 reference aircraft to  
 175 the same wing area and mass, the corresponding mass scaling exponent is  $\kappa = 3.23$ . The airframe of the improved MX2 design aimed at  $m_{MX2} = 1852\text{kg}$  for a wing area of  $A_{MX2} = 54\text{m}^2$ , equivalent to  $\kappa = 2.719$  relative to the AP2 reference. Similarly, WT mass scales with an exponent slightly below 3 based on rotor diameter (Fingersh et al., 2006).

$$m_{\text{scaled}} = m_{\text{ref}} \left( \frac{b}{b_{\text{ref}}} \right)^{\kappa}; \quad \mathbf{J}_{\text{scaled}} = \mathbf{J}_{\text{ref}} \left( \frac{b}{b_{\text{ref}}} \right)^{\kappa+2} \quad (4)$$

### 3.5 Tether model

~~moved sub-section~~ The tether is modeled as a [straight, cylindrical single](#) solid rod [with constant diameter](#) which can not support compressive forces. This is a good assumption when tether tension is high during the power production phase of the power cycle. Total tether drag is proportional to tether diameter  $d_{\text{tether}}$  and tether length  $l_{\text{tether}}$ . Both scale with tether tension, assuming a constant tensile strength, and therefore aircraft size and wind speed (see subsection 4.6). The tether drag is approximated by dividing the tether into multiple elements (here  $n_{\text{tether}} = 10$ ) and calculating the apparent wind speed at  
 185 each element individually, assuming a constant tether drag coefficient of  $C_D^{\text{tether}} = 1$ , [which could even be higher for braided tethers](#). Each elements tether drag is then equally divided between the two endpoints and finally transferred to either the aircraft or ground station. ~~However,~~ This leads to an underestimation of total tether drag at the aircraft (Leuthold et al., 2018).

Similarly, the total tether weight  $W_{\text{tether}}$ , calculated with a constant material density of  $\rho_{\text{tether}} = 970 \text{kgm}^{-3}$ , is distributed evenly between the aircraft and ground station.

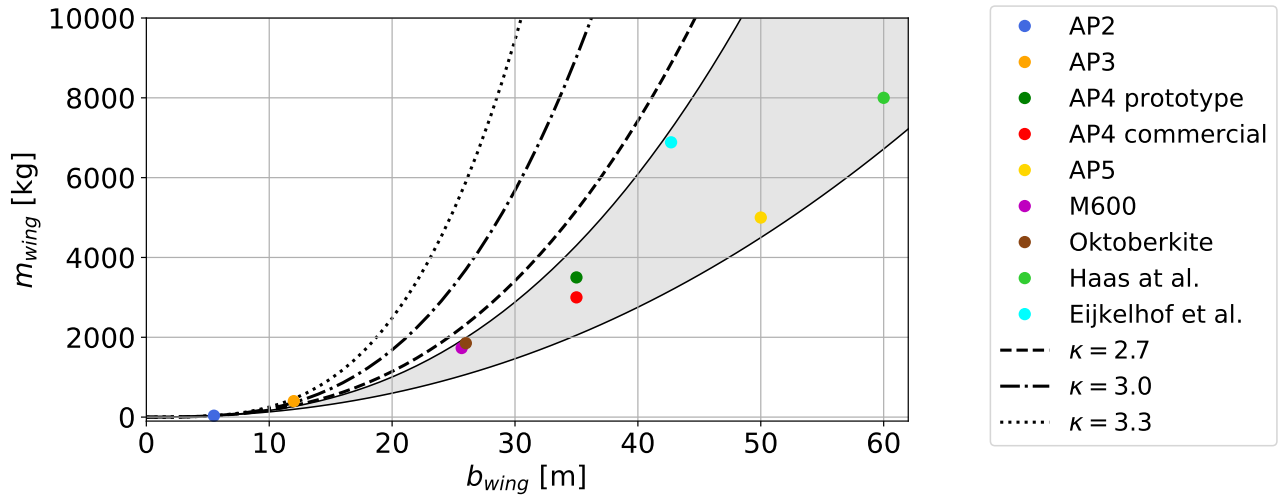


**Figure 3.** [Curve fit of published sizing study AWES aircraft mass](#) Haas et al. (2019); Kruijff and Ruiterkamp (2018); Eijkelhof et al. (2020); Ampyx (2020); Echeverri et al. (2020). [For these data mass scales within a scaling exponent range of  \$\kappa = 2.2 - 2.6\$  \(grey area\). The investigated, more conservative, mass scaling exponents between  \$\kappa = 2.7 - 3.3\$  are depicted by dashed, dash-dotted and dotted lines.](#)

190 Tether force constraints are chosen such that the system's rated power is achieved for a logarithmic wind speed profile with  $U_{\text{sizing}}(z = 200 \text{ m}) \approx 10 \text{ ms}^{-1}$  ( $U_{\text{sizing}}(100 \leq z \leq 400 \text{ m}) \approx 10 \text{ ms}^{-1}$ ), similar to wind at hub height for conventional wind turbines. [Therefore, the tether diameter of every AWES design \(table 2\) is derived from the maximum tether stress  \$\sigma\_{\text{tether}} = 3.6 \cdot 10^9 \text{ Pa}\$  and a safety factor  \$SF\_{\text{tether}} = 3\$ . The tether diameter is calculated assuming a maximum allowable tether stress  \$\sigma\_{\text{tether}} = 3.6 \cdot 10^9 \text{ Pa}\$  and a safety factor  \$SF\_{\text{tether}} = 3\$ .](#)

195 [The Ground station is not explicitly modeled, instead hypothetical tether speed and acceleration constraints are imposed, mimicking motor torque and rotational speed limitations. Maximum reel-out speed is limited to  \$v\_{\text{out}} = 15 \text{ ms}^{-1}\$  and reel-in speed to  \$v\_{\text{out}} = 10 \text{ ms}^{-1}\$ . This limits the mechanical, instantaneous power that each ground-generation AWES can generate  \$P\_{\text{inst}}^{\text{max}} = F\_{\text{tether}}^{\text{max}} v\_{\text{out}}\$ . A maximum tether acceleration of  \$\ddot{l} = 10 \text{ ms}^{-2}\$  is imposed to comply with generator torque limits.](#)

### 3.6 Aerodynamic scaling

200 Figure 5 [shows compares](#) the aerodynamic performance of the AP2 wing model [with and without a 500m tether to a high lift wing, which includes](#) Lift  $C_L$  (top-left a), drag  $C_D$  (top-center b) and pitch moment  $C_m$  coefficients (top-right c) [as a function of angle of attack  \$\alpha\$ , Lift over drag \(bottom-left d\) and glide ratio are depicted](#) as a function of angle of attack (bottom-center e). [Lift over Drag is shown in \(d\). The bottom right figure \(f\) shows displays](#) the  $\frac{C_{LR}^3}{C_D^2}$  ratio (equation 1) which determines the theoretical maximum power of any crosswind AWES (Loyd, 1980; Diehl, 2013). Makani's reports mention two shortcomings

205 of their M600 design were the overestimation of  $C_L^{\text{max}}$  and underestimation of  $C_D$ , further justifying this comparison and

prompting a more conservative estimation of practical aerodynamic coefficients. [The aerodynamic coefficients of the AP2 reference model were identified in AVL](#) (Drela and Youngren, 2016) [CFD analyses by Ampyx Power and during untethered test flights](#). (Malz et al., 2019) Modifications to the AP2 aerodynamic reference model were implemented to assess the impact of improved aerodynamics [performance on AWES performance \(labeled HL for high lift\)](#). This is achieved by shifting the  $C_L$ ,  $C_D$  and  $C_m$  [according to their theoretical behaviour](#) as if high lift devices, such as [fixed trailing-edge flaps and slats](#) [fixed leading-edge slots](#), were attached.[added new ref:](#) Kermode et al. (2006); Lee and Su (2010); Hurt (1965); Scholz (2016). Lift and drag at zero angle of attack are increased, stall is delayed, and pitch moment decreased. While both airfoils have comparable optimal glide ratios, the Loyd's optimal power ratio is almost twice as high for the high lift airfoil. Stall effects were implemented for both the AP2 reference model (blue) as well as the high lift (HL - orange) model by formulating a quadratic lift coefficient function (see figure 5). As a result, the lift coefficients deviate slightly in the linear lift region at lower angle of attack.

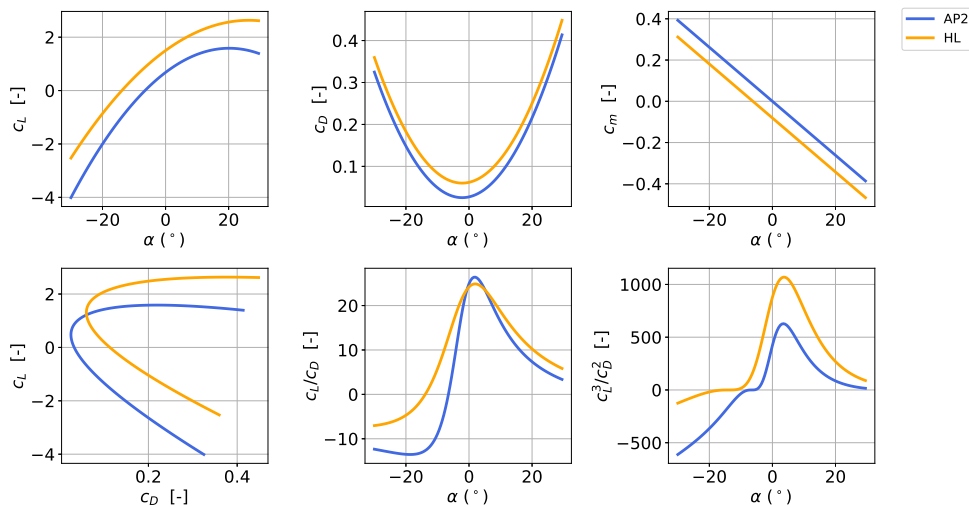


**Figure 4.** Aerodynamic lift  $C_L$ , drag  $C_D$ , pitch-moment  $C_m$  coefficients as a function of angle of attack for reference AP2 (blue) and high-lift (HL) (orange). HL is derived by modifying the AP2 reference model, in accordance with the theoretical, as if high-lift devices, e.g. flaps and slats were attached.

### 3.7 Constraints

As previously mentioned, the AWES model solves a [constraint](#) optimal control problem to maximize average cycle-power [of a single 6 DOF tethered aircraft connected to the ground station via a single rigid tether](#). Each run optimizes the trajectory [during the production cycle of an AWES at a fixed size subject to varying wind conditions](#). **These** Constraints include system dynamics, material properties, aircraft [\(sub-section 3.6\)](#) and ground station hardware constraints as well as flight envelope limitations [listed in table 2](#) [More information on the model and constraints can be found under](#) awebox (2020) [and](#)

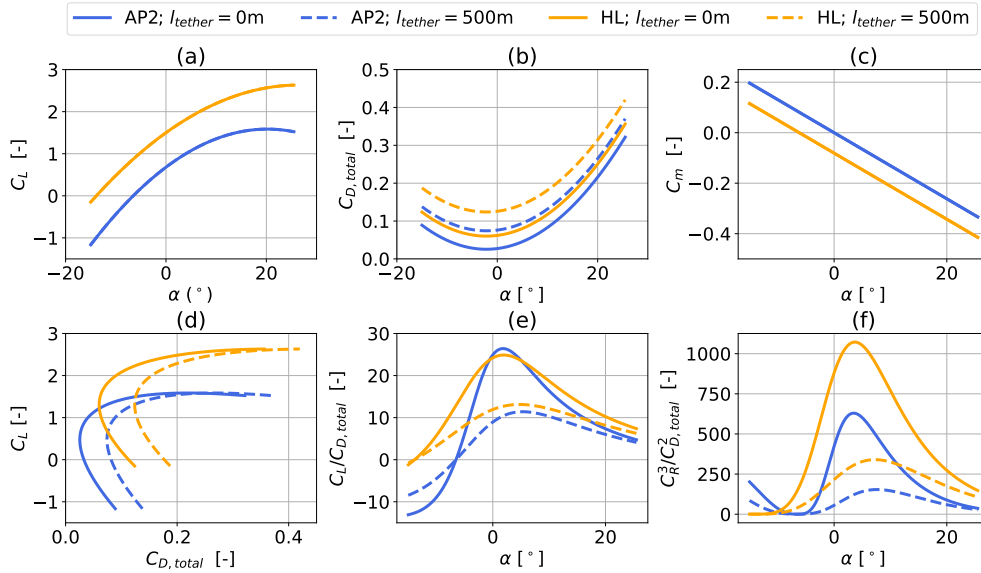


**Figure 5.** Aerodynamic lift  $C_L$  (a), drag  $C_D$  (b), pitch moment  $C_m$  coefficients (c) and with (dashed line) and without tether drag (solid line) as a function of angle of attack for AP2 (blue) (Malz et al., 2019) and high-lift (HL) (orange) configuration. The bottom sub-figures display lift over drag (d), lift to drag ratio over angle of attack (e) and  $C_R^3/C_{D,total}^2$  over angle of attack according to Loyd Loyd (1980). HL coefficients are derived by modifying the AP2 reference model as if high-lift devices, e.g. flaps and slats were attached.

the referenced publications. These limitations contain a include minimum and maximum operating heights ( $z_{operation}^{min}$  and  $z_{operation}^{max}$ ), maximum acceleration measured as multiples of  $g$   $a_{flight}^{max}$ , as well as a maximum tether length  $l_{tether}^{max}$  to maintain safe operation. The number of loops  $n_{loop}$  within each cycle is fixed to 5. Additionally, an apparent flight speed constraint of  $v_{app} \leq 80 \text{ ms}^{-1}$  was imposed to reduce the mechanical wing load. The maximum tether stress and force, from which the tether diameter is calculated, together with the periodicity constraint are some of the most important path constraints. Ground station hardware limitations such as torque and acceleration dynamics are not explicitly modeled, but implemented as tether speed and acceleration constraints. A fixed angle of attack  $\alpha$  and side slip angle  $\beta$  range ensures operation within realistic bounds. However, neither angular constraint is active during flight, because the optimizer tries to achieve an angle of attack close to the maximum of  $C_L$ ,  $C_D$  and  $C_m$  (see figure 5). Due to weight and drag effects, actual angle of attack is closer to  $\alpha \approx 10^\circ$  during reel-out for the majority of wind speeds. Table 2 summarizes constraints and system sizes.

**Table 1.** List of [investigated](#) AWES design parameters [and selected, important system constraints.](#) [with AP2 reference](#)

Parameter	AP2	<a href="#">size design 1</a>	<a href="#">size design 2</a>	<a href="#">size design 3</a>	<a href="#">size design 4</a>	<a href="#">size design 5</a>	<a href="#">size design 6</a>
$A_{wing}$ [m <sup>2</sup> ]	3	10	20	50	80	100	150
$c_{wing}$ [m]	0.55	1.00	1.41	2.24	2.83	3.16	3.87
$b_{wing}$ [m]	5.5	10	14.1	22.4	28.3	31.6	38.7
Aircraft AR [-]	10	10	10	10	10	10	10
$m_{kite}(\kappa = 2.7)$ [kg]	36.8	185	471	1,624	3,062	4,139	7,155
$m_{kite}(\kappa = 3.0)$ [kg]	36.8	221	626	2,473	5,005	6,995	12,850
$m_{kite}(\kappa = 3.3)$ [kg]	36.8	265	830	3,767	8,180	11,821	23,079
$\alpha$ [°]					[-10 : 30]		
$\beta$ [°]					[-15 : 15]		
Tether $l_{tether}^{max}$ [m]					2000		
$\dot{l}_{tether}$ [ms <sup>-2</sup> ]					[-15 : 10]		
$\ddot{l}_{tether}$ [ms <sup>-2</sup> ]					[-15 : 10]		
$\ddot{l}_{tether}^{max}$ [ms <sup>-3</sup> ]					<del>20</del> [-20 : 20]		
$\rho^{tether}$ [kgm <sup>-3</sup> ]					970		
$\sigma_{max}^{tether}$ [Pa]					3.6 10 <sup>9</sup>		
$SF^{sigma}$ [-]					3		
$d_{tether}(AP2)$ [mm]		5.5	7.8	12.3	15.5	20	21.7
$d_{tether}(HL)$ [mm]		7.2	10.2	16.1	20.6	23	28.3
$F_{tether}^{max}(AP2)$ [kN]		34	60	136	241	377	456
$F_{tether}^{max}(HL)$ [kN]		46	94	241	416	499	738

**Table 2.** List of [investigated](#) AWES design parameters [and selected, important system constraints.](#) [with AP2 reference](#)

Parameter	AP2	<a href="#">size design 1</a>	<a href="#">size design 2</a>	<a href="#">size design 3</a>	<a href="#">size design 4</a>	<a href="#">size design 5</a>	<a href="#">size design 6</a>
flight envelope $z_{operating}^{min}$ [m]		55	60	75	90	100	125
$z_{operating}^{max}$ [m]					1000		
$v_{flight}^{max}$ [ms <sup>-1</sup> ]					80		
$a^{max}$ [g]					12		
$n_{loop}$ [-]					5		
Initialization $N_{loops}$					5		
$\epsilon$ [°]					30		
$l_{tether}^{init}$ [m]		500	535	643	750	821	1000

### 3.8 Initialization

The AWES dynamics are highly non-linear and therefore result in a non-convex optimal control problem which possibly has multiple local optima. Therefore, the particular results generated by a numerical optimization solver can only guarantee local optimality, and usually depend on the chosen initialization. The optimization is initialized with a circular trajectory based on a fixed number of  $n_{\text{loops}} = 5$  loops at a  $30^\circ$  elevation angle and an estimated aircraft speed of  $v_{\text{init}} = 10 \text{ ms}^{-1}$ . Previous analyses showed that the convergence of large AWES highly depends on initial tether length. Larger systems become less sensitive to tether drag and hence can drag along a longer tether, because lift to tether drag ratio scales linearly with wing span. Therefore, initial tether length is increased linearly with aircraft wing area (see table 2).

In order to solve the highly nonlinear optimization problem, an appropriate initial guess is generated using a homotopy method similar to those detailed in (Gros et al., 2013; Malz et al., 2020). This technique gradually relaxes the problem from simple tracking of circular loops to the original nonlinear path optimization problem where the previous result serves as an initial guess for the following problem. [An initial circular path, which is determined from the tether length guess and estimated flight speed, is transformed into a periodic helix-like trajectory. Several initial tether lengths were investigated to determine a feasible initial path depending on system mass, system size and wind speed. Initial tether lengths needs to increase with system size and wind speed.](#) The resulting problem is formulated in the symbolic modeling framework CasADi for Python (CasADi, 2016; Andersson et al., 2012) and solved using the NLP solver IPOPT (Wächter and Biegler, 2006) in combination with the linear solver MA57 (HSL, 2020).

**Table 3.** List of AWES optimization initialization values

Parameter		design 1	design 2	design 3	design 4	design 5	design 6
Initialization	$N_{\text{loops}}$			5			
	$\varepsilon [^\circ]$			30			
	$l_{\text{tether}}^{\text{init}} [\text{m}]$	500	535	643	750	821	1000

We compare 6 AWES sizes with three different mass properties and two sets of nonlinear aerodynamic coefficients each to investigate the AWES design space and upscaling potential. Furthermore, we contrast AWES performance at representative onshore (Pritzwalk in northern Germany) and offshore locations (FINO3 research platform in the North Sea) based on one year of WRF simulated and k-means clustered wind data. To that end, we show representative optimized trajectories (subsection 4.1) and compare typical operating altitudes and tether lengths (subsection 4.2). We estimate reaction forces and bending moments based on the assumption of an elliptical lift distribution (subsection 4.3). Subsection 4.4 analyses AWES power curves for each design and determines an AWES power coefficient based on swept area and wing chord. From this we derive the annual energy production (AEP) in subsection 4.5 for each location and system configuration. We examine the predicted power losses (subsection 4.7) due to tether drag. Finally, we establish an upper limit of the weight to lift ratio and compare tether drag forces in subsection 4.6.

#### 4.1 Flight trajectory and time series results

~~Due to the high level of model and problem non-linearity, the solution of the optimization algorithm can only guarantee local optimality. However, The generated The trajectories, shown in Figures 6 and A1 (center) for a representative AWES with a wing area of  $A_{\text{wing}} = 50 \text{ m}^2$  and  $\kappa = 3$  and seem reasonable, are within the set constraints, and are consistent with other studies (De Schutter et al., 2019; Sommerfeld, 2020) which use the same model. The trajectories in sub-figure b) and d) of Figure 6 depict the local optima of the highly non-linear model and optimization problem for AWESs with a wing area of  $A_{\text{wing}} = 50 \text{ m}^2$ , both AP2 (solid lines) and HL (dashed lines) aerodynamic coefficients and  $\kappa = 3$ . The trajectories seem reasonable, are within the set constraints, and are consistent with other studies (De Schutter et al., 2019; Sommerfeld, 2020) which use the same model.~~

Sub-figure a) of Figure 6 shows the wind speed profiles  $U$  over altitude  $z$  with the operating region highlighted in color. Any deviation from the WRF data in grey is caused by the interpolation with Lagrange polynomials during the implementation process described in subsection 3.3. The hodographs in sub-figure c) show a top view of the rotated wind velocity components  $u$  and  $v$  up to a height of 1000 m which follow the expected clockwise rotation with altitude (Stull, 1988). The average wind speed between  $100 \text{ m} \leq z \leq 400 \text{ m}$  is used as reference wind speed  $U_{\text{ref}}$ , as it is a good enough proxy for conditions at operating height (Sommerfeld, 2020).

~~It is striking that higher wind speed~~ Trajectories at higher wind speeds and above rated power ~~often~~ deviate noticeably from the expected trajectory, which manifest at lower wind speeds. The system tries to de-power by moving out of the wind window, either upwards or perpendicular to the main wind direction, to stay ~~with-in~~ within the tether force, tether speed and flight speed constraints, while still maximizing average power. Subsection 4.2 further analyzes the trend towards longer tethers and higher operating altitude with increasing wind speed, which can be seen here as distance from the origin.

~~The top-left sub-figure in figure 7 shows the wind speed profiles  $U$  over altitude  $z$  (top) with the operating region highlighted in color. Any deviation from the WRF data in grey is caused by the interpolation with Lagrange polynomials during the~~

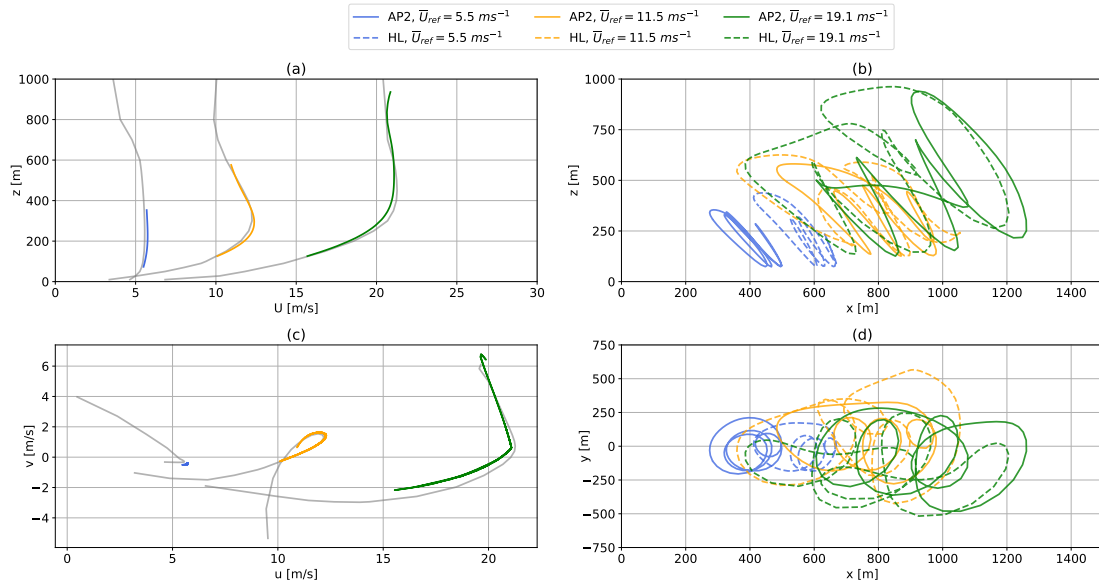


**Figure 6.** Optimization results of ground-generation AWES with a wing area of  $A_{wing} = 50 \text{ m}^2$ , mass scaling exponent  $\kappa = 3$  for both AP2 reference (solid lines) and high-lift HL (dashed lines) aerodynamic coefficients at various WRF-generated wind conditions. Sub-figure (a) and (c) depict representative horizontal onshore wind speed profiles and their hodographs of wind velocity up to 1000 m. The deviation of the colored lines is caused by the implementation of discrete WRF-simulated data points using Lagrange polynomials. Sub-figure (b) and (d) show the optimized trajectories in side and top view.

implementation process described in subsection 3.3. The hodograph in the bottom left sub-figure shows a top view of the rotated wind velocity components  $u$  and  $v$  up to a height of 1000 m which follow the expected clockwise rotation with altitude (Stull, 1988).

The four sub-figures on the right display the lift force  $L$ , tether speed  $v_{tether}$ , the apparent, constrained wind speed  $v_{app}$  and the instantaneous power  $p_{current}$  time series for the corresponding trajectories. Both the production (reel-out) and recovery phase (reel-in) are clearly distinguishable by the transition to negative tether speed and power. Figure 8 describes the time-dependent attitude of the previously analyzed trajectories during the operating cycle. **Markus: Comment this in response to reviewers because it has changed now!** Total cycle time seems independent of wind speed and solely determined by the number of loops and tether length used to initialize the optimization. Cycle time varies with wind speed and system configuration. A possible explanation is that better aerodynamics lead to higher flight speed and therefore shorter time to complete the cycle, as can be seen for lower wind speeds ( $\bar{U}_{ref} = 5.5 \text{ ms}^{-1}$ , blue). At higher wind speeds however, the system reduces its flight speed to stay within constraints, leading to a longer cycle time. The algorithm maintains a fixed number of loops, resulting in unnecessary and probably less optimal trajectories during the reel-in period, as can be seen for HL  $U_{ref} = 11.5$  and  $19.1 \text{ [ms}^{-1}]$  at around 100 seconds. Our previous analyses, utilizing the same model, However, previous investigations showed that AWES power

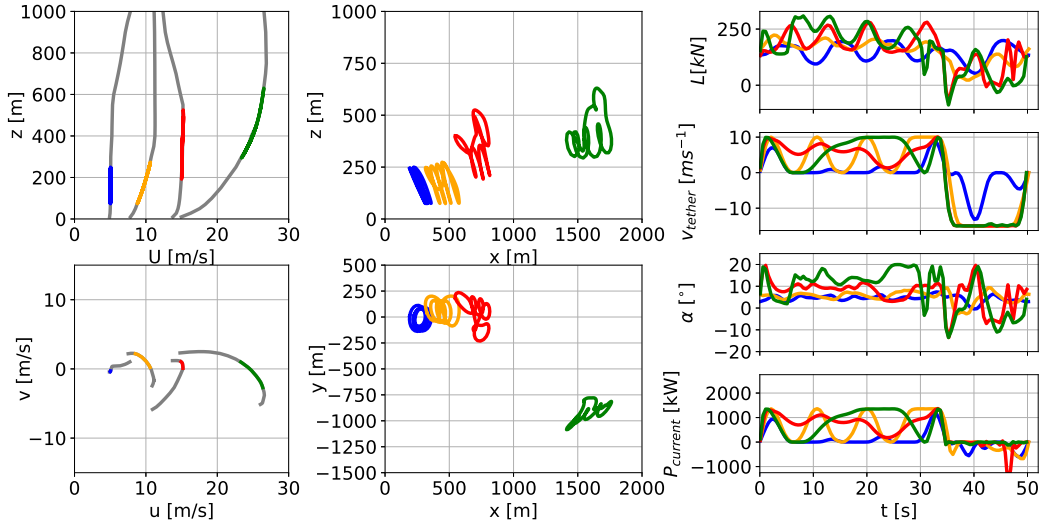


**Figure 7.** Optimal trajectory and time-series for a ground-generation AWES with a wing area of  $A_{\text{wing}} = 50 \text{ m}^2$ , mass scaling exponent  $\kappa = 3$  and AP2 reference aerodynamic coefficients. The left subfigures display representative wind speed profiles (top), and hodograph of wind velocity up to 1000 m (bottom). The deviation of the colored lines is caused by the implementation of discrete WRF-simulated data points using Lagrange polynomials. Trajectories (center) in side and top view. The right subfigures show aerodynamic lift  $L$ , tether speed  $v_{\text{tether}}$ , angle of attack  $\alpha$  and instantaneous power  $P_{\text{current}}$  time series, optimized subject to the corresponding wind velocity profiles.

output seems to be insensitive to both number of loops (here  $n_{\text{loop}} = 5$  for all setups) and flight time. [However, this needs to be verified and compared to other models and real experiments.](#)

300 [Markus: Make sure that this is not a repetition.](#) The optimizer aims to achieve a constant tether force  $F_{\text{tether}}$  during the reel-out period, resulting in a constant tether force (a) at higher wind speeds. At lower wind speeds, this can not be achieved, because the aircraft can not produce sufficient lift force to pull the tether and overcome gravity during the ascent within each loop of the production cycle. As a result, tether force decreases together with apparent wind speed  $v_{\text{app}}$  (c), tether speed  $v_{\text{app}}$  (b) and instantaneous power  $P_{\text{current}}$  (e) (see  $U_{\text{ref}} = 5.5 \text{ [ms}^{-1}\text{]}$ , blue). Even at higher wind speeds (see  $U_{\text{ref}} = 11.5 \text{ [ms}^{-1}\text{]}$ , orange) the tether speed drops to zero at during the ascent. Additionally, tether force decreases with tether length during the ascent, due to increased total system weight. To alleviate this inherent intermittency, buffering the energy or coupling multiple, phase-shifted AWES in a wind farm setup would be beneficial (Malz et al., 2018).

310 The diverse AWES trajectories generate periodic aerodynamic forces and tether tension. In the production phase, the tether reels-out and the aircraft follows an almost circular pattern, which leads to deceleration during the ascent and acceleration during the descent. To maintain tether tension, tether speed decreases to zero. As a consequence, the generated power also drops to zero and ramps up again (figure 8 (e)), leading to feed-in challenges. To alleviate this inherent intermittency, buffering the energy or coupling multiple, phase-shifted AWES in a wind farm setup could be beneficial (Malz et al., 2018). [Additionally,](#)

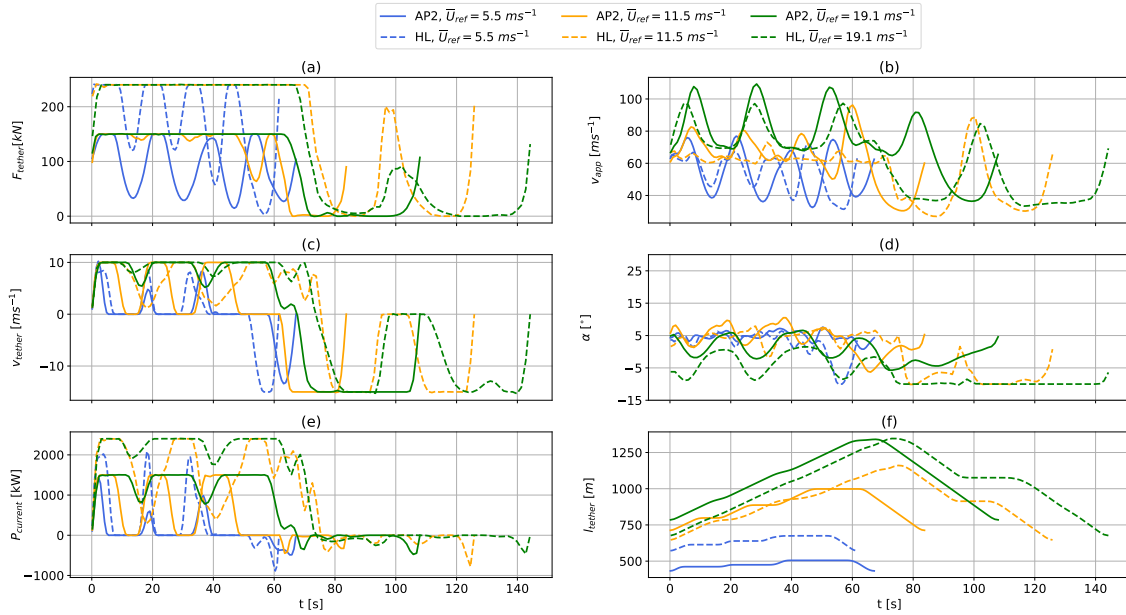


**Figure 8.** Time series of optimized ground-generation AWES with a wing area of  $A_{\text{wing}} = 50 \text{ m}^2$ , mass scaling exponent  $\kappa = 3$  for both AP2 reference (solid lines) and high-lift HL (dashed lines) aerodynamic coefficients at various WRF-generated wind conditions. The corresponding trajectories are shown in Figure 6. The sub-figures show tether force  $F_{\text{tether}}$  (a), tether speed  $v_{\text{tether}}$  (c) and instantaneous power  $P_{\text{current}}$  (e), as well as apparent wind speed  $v_{\text{app}}$  (b), angle of attack  $\alpha$  (d) and tether length  $l_{\text{tether}}$  (f).

aerodynamic loads drop to almost zero during the recovery phase as the aircraft returns to its initial position and the tether is reeled in. To reduce the power losses and decrease the reel-in time, tether speed quickly reaches its minimum of  $v_{\text{tether}} = 15 \text{ ms}^{-1}$ .

315 At lower wind speeds, aerodynamic forces oscillate about a constant base load (figure 8) during the reel-out phase. With increasing wind speed, aerodynamic forces saturate due to tether tension constraints (table 2), leading to increasing periods of constant, maximum tension. Figure 9 gives an insight into the tether load cycles during the reel-out phase of an AWES with a wing area of  $A_{\text{wing}} = 50 \text{ m}^2$ , both AP2 and HL aerodynamic coefficients and mass scaling of  $\kappa = 2.7, 3.0, 3.3$ . **ADD: a),b); check period of smaller and larger AWES (maybe need to do in Ubuntu?** Average time between troughs (a) slightly  
 320 increases with  $\kappa$  due to increased aircraft inertia, but remains almost constant with wind speed  $U_{\text{ref}} (100 \text{ m} \leq z \leq 400 \text{ m})$ . The relative decrease in tether tension ( $\Delta F_{\text{tether}}/F_{\text{tether,max}}$ , (b)) decreases with wind speed as the apparent wind speed increases. As expected this decrease is more pronounced for heavier AWES. Higher aerodynamic efficiency (HL circular marker and dotted line) increases performance and smooths out the troughs. The lightest configuration achieves constant reel-out tension at around rated wind speed of  $U_{\text{ref}} = 10 \text{ ms}^{-1}$ , while the heaviest design requires higher wind speeds of about  $15 \text{ ms}^{-1}$ .

325 Looking at the periodic nature of the lift force gives an insight into the load cycles AWES need to withstand during long-term operation. During the production phase the aerodynamic loads oscillate about a constant base load with a periodicity of

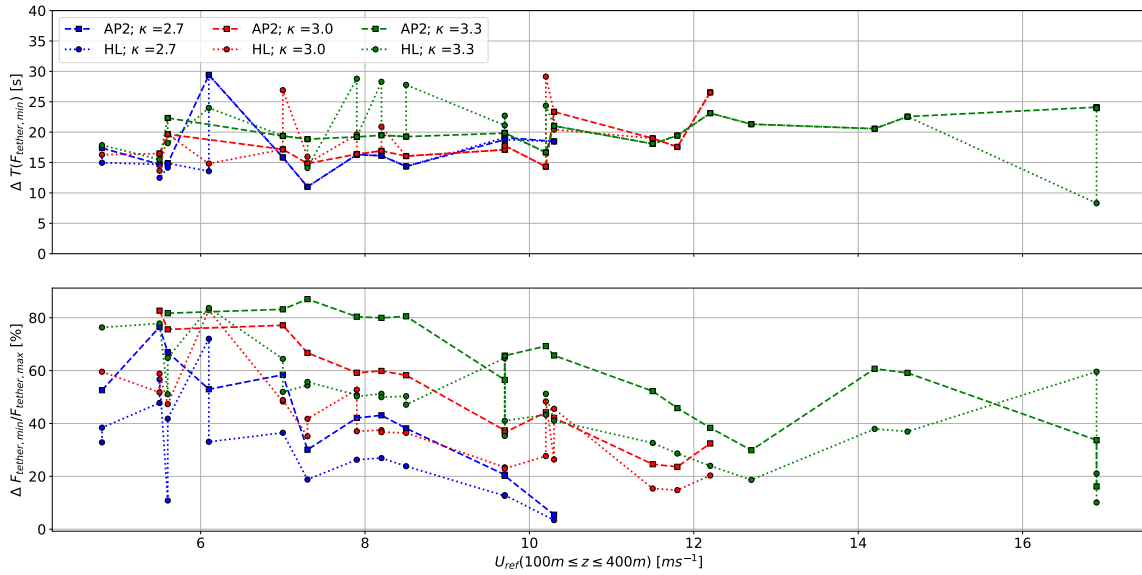


**Figure 9.** Markus: add underline because average Average time between tether tension troughs (a) and relative decrease in tether tension (b) during the production phase of optimized ground-generation AWES with a wing area of  $A_{\text{wing}} = 50 \text{ m}^2$ . The figures show results for mass scaling exponents  $\kappa = 2.7, 3.0, 3.3$  (blue, red, green) and both sets of aerodynamic coefficients AP2 reference (square, dashed line) and high-lift HL (circle, dashed lines).

approximately 8 to 15 seconds depending on aircraft size and wind speed which is comparable to the rotational speed of a conventional wind turbine. Additionally, aerodynamic loads drop to almost zero during the recovery phase as the aircraft returns to its initial position and the tether is reeled in. Subsection 4.3 further investigates the resulting wing peak loads:

330 During the production phase tether speed repeatedly drops to zero for an extended period of time, especially at lower wind speeds. This is caused by insufficient lift during the ascent of the aircraft as the system can not produce enough aerodynamic force to pull the tether and overcome gravity. Simultaneously as a consequence power drops to zero and ramps up again, following the flight cycle. To alleviate this inherent intermittency, buffering the energy or coupling multiple, phase-shifted AWES in a wind farm setup would be beneficial (Malz et al., 2018). The reel-out speed only remains positive during the entire

335 production phase at higher wind speeds or for aircraft with higher aerodynamic lift. During the recovery phase tether speed quickly reaches its minimum of  $v_{\text{tether}} = 15 \text{ ms}^{-1}$  to keep this phase as short as possible and reduce power loss. The angle of attack remains moderate to stay close to optimal  $\frac{C_{LR}^3}{C_{D,\text{total}}^2}$ . However, the angle of attack is generally higher than the theoretical optimum to offset the weight and drag of the entire system:

## 4.2 Tether length and operating altitude

340 One of the major value propositions of AWESs is that they can tap into wind resources beyond the reach of conventional wind turbines. However, the choice of optimal operating height highly depends on the wind speed profile and system design. Two opposing effects influence the optimal operating height. On the one hand, an increase in altitude is generally associated with an increase in wind speed and therefore produced power. On the other hand, higher altitudes require a longer tether which results in higher drag losses **and also** or increase the elevation angle which increase **gravity-caused** “cosine” losses (Diehl, 2013) or  
 345 both.

Figure 10 shows a trend towards longer average tether lengths  $\bar{l}_{\text{tether}}$  (top) and higher average operating altitudes  $\bar{z}_{\text{operating}}$  (center) with increasing system size for a representative scaling exponent of  $\kappa = 3$  (see equation (4)) and wind speed. We chose  $U_{\text{ref}}$  to be the average wind speed between  $100 \text{ m} \leq z \leq 400 \text{ m}$  as we previously found that this range is a good proxy for conditions at operating height (Sommerfeld, 2020). Lighter aircraft and higher lift wings results in slightly higher operating  
 350 altitudes, a longer tether and higher elevation angle (compare figure A2 in the appendix).

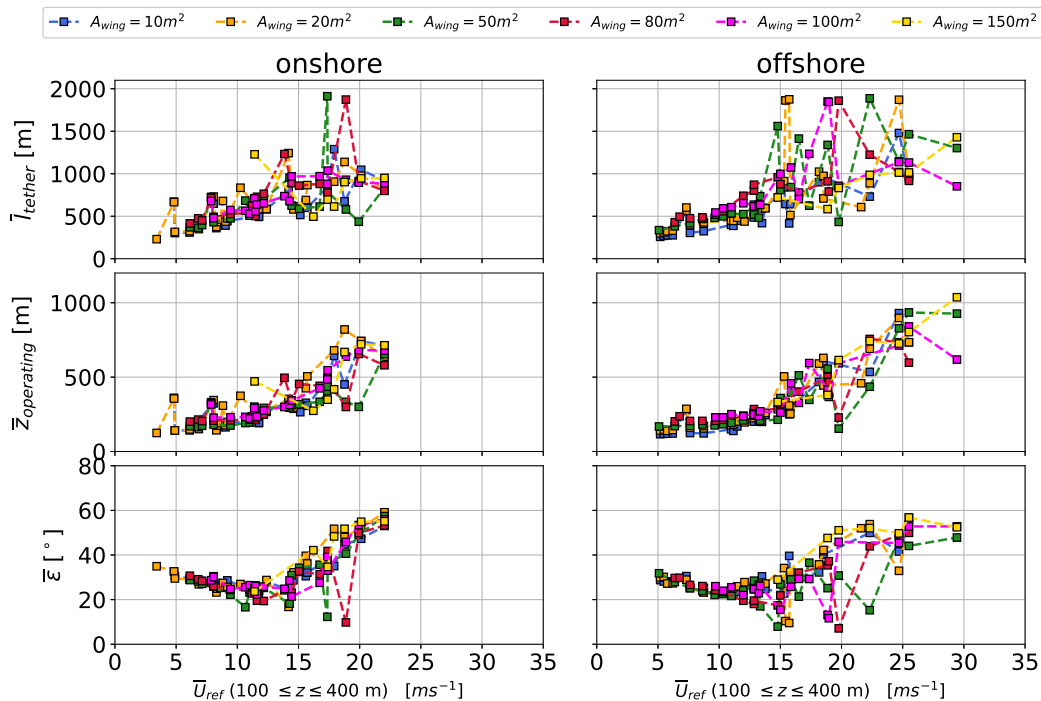


**Figure 10.** Average tether length  $\bar{l}_{\text{tether}}$  (top), average operating altitude  $\bar{z}_{\text{operating}}$  (center) and average elevation angle  $\bar{\varepsilon}$  (bottom) over reference wind speed  $\bar{U}_{\text{ref}} (100 \leq z \leq 400 \text{ m})$ . Results for wing areas between  $A_{\text{wing}} = 10 - 150 \text{ m}^2$  scaled with a mass scaling exponent of  $\kappa = 3$ , AP2 reference aerodynamic coefficients for both onshore (left) and offshore (right) location.

Outliers, e.g. for high wind speed profiles (compare figure 2), are likely local optima of the highly nonlinear trajectory optimization problem described in section 3.

As wind speed increases beyond rated power ( $U_{\text{ref}} \approx 10 \text{ ms}^{-1}$ , see figures 12 and A3), the aircraft moves out of the wind window to de-power. This is seen as rising average elevation angles  $\bar{\varepsilon}$  (bottom) above  $U_{\text{ref}} = 10 \text{ms}^{-1}$ . Results for both offshore (right) and onshore (left) follow the same trends, but operating heights below rated wind speed are lower offshore because of lower wind shear and higher wind speeds.

It is important to keep in mind that even though the operating height exceeds 500 m for wind speeds of more than  $U_{\text{ref}} \approx 15 \text{ ms}^{-1}$  such wind speeds occur only about 10 % of the time (see figure 2). Between 5 and  $15 \text{ ms}^{-1}$ , the most likely wind speed range, operating heights both onshore and offshore are between 200 to 300 m. For smaller system sizes these heights are even lower. While this is slightly above the hub-height of current conventional wind turbines, it rebuts the argument of harvesting wind energy beyond this altitude. These findings are consistent with current offshore WT trends, whose rotor diameter increased significantly while hub height only increased marginally over the last years. However, it is likely that offshore hub heights will increase as technology improves, making the argument for the deployment of AWES particularly challenging as both operate at comparable heights and WT are the more proven and established technology. However, this might be different for multiple kite systems which could benefit from longer tethers, due to reduced tether motion (De Schutter et al., 2019).

### 4.3 Reaction forces and moments

~~We analyze wing loads since detailed design of the aircraft and wing box is beyond the scope of this paper. Weight is neglected as it is an order of magnitude smaller than the aerodynamic lift force. We assume an elliptic lift distribution (equation: (5) (Torenbeek and Wittenberg, 2009)) which results in a normalized line load of  $\tilde{l}$ , normalized shear force  $\tilde{V}_{\text{Lift}}$  and normalized bending moment  $\tilde{M}_{\text{Lift}}$ . Loads are normalized by their maximum value at the wing root ( $l_0, V_0, M_0$ ) to obtain generalized trends independent of wing size.~~

$$l = l_0 \sqrt{1 - (\tilde{y})^2} \quad (5)$$

~~Figure 11 visualizes the maximum cycle-average loads at the wing root, which can be used to scale the normalized load distributions along the wing, for both sets of aerodynamic coefficients, all three mass scaling exponents  $\kappa$  and aircraft wing area  $A_{\text{wing}}$ . Aerodynamic line loads  $l_0$  (top) scale favorably with wing area as they only scale with wing span while total lift force  $V_0$ , equivalent to total shear force  $V$ , scales linearly with wing area. In contrast, bending moment  $M_0$  scales with area and wing length.~~

~~Higher aerodynamic lift coefficients (HL: circle) result in higher aerodynamic loads in comparison to the AP2 reference model (AP2: square). Heavier aircraft with higher mass scaling exponent  $\kappa$  (subsection 3.4) also result in higher aerodynamic loads as they require more lift to ascent which results higher average aerodynamic forces. Data for an aircraft with an area of  $A_{\text{wing}} = 150 \text{ m}^2$  and  $\kappa = 3.3$  are missing as the optimization could not find a feasible solution.~~

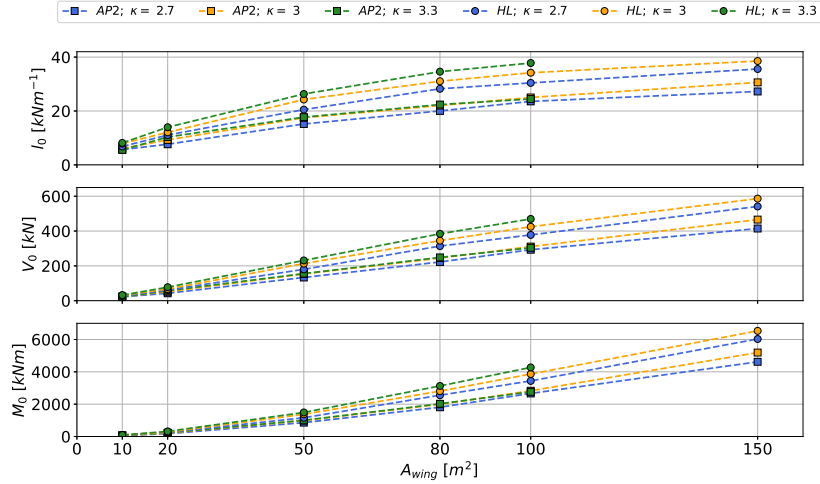


**Figure 11.** Maximum cycle-averaged aerodynamic line load  $l_0$  (top), lift force  $V_0$  (center) and bending moment  $M_0$  (bottom) at the wing root over wing area  $A_{wing}$ . Summarizes data for both sets of aerodynamic coefficients (HL: circle, AP2: square) and all three mass-scaling exponents  $\kappa = 2.7, 3, 3.3$ .

#### 4.4 Power curve [annual energy distribution and power harvest factor](#)

This section investigates a representative cycle-average AWES power curve for all sizes and estimates an AWES power coefficient  $c_p^{AWES}$  as a function of swept area. For visualization purposes, only data for the offshore location, a mass-scaling exponent of  $\kappa = 2.7$  and HL aerodynamic coefficients are shown here. Other results follow similar trends. Some can be found in the appendix in figure 12 and A3.

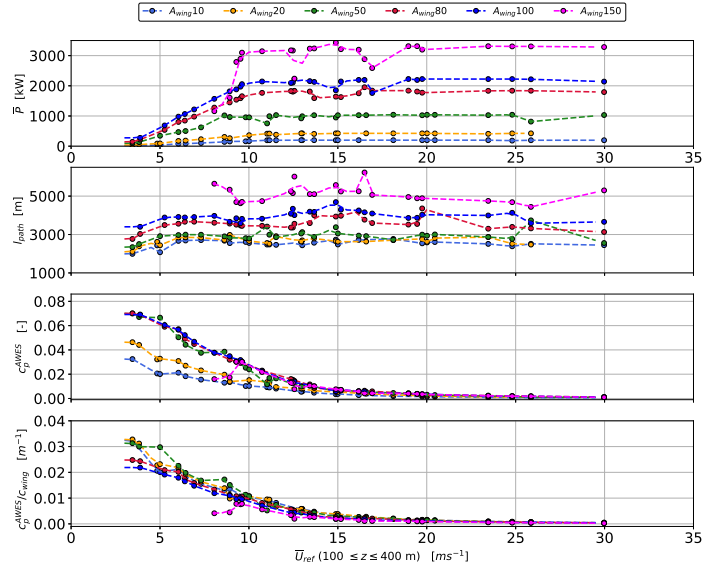
Plotting the cycle-average power  $\bar{P}$ , derived from 3 representative profiles from each of the 10 wind velocity clusters, over reference wind speed produces typical wind power curves as seen in figure 12 (top). As of now, no standard reference wind speed  $U_{ref}$ , equivalent to wind speed at hub height for conventional WT, has been agreed upon for AWES. Furthermore, using this altitude range results in comparable power curve trends onshore and offshore.

Table 4 summarizes the rated power  $\bar{P}_{rated}$  for AWES between 10 and 150  $m^2$  scaled with a mass-scaling exponent of  $\kappa = 2.7$ . The table also displays the equivalent WT rotor diameter  $D_{WT}^{equiv}$ , for an assumed power coefficient of  $c_p^{WT} = 0.4$  and a rated wind speed of  $10ms^{-1}$ , as reference. The system size and therefore material cost benefits of AWES become obvious when comparing AWES wing span  $b_{wing}$  to WT rotor diameter  $D_{WT}^{equiv}$ . AWES wing span is about 30 (HL) to 40% (AP2) of the equivalent rotor diameter.

Missing data in figure 12 originate from an infeasible combination of constraints and boundary conditions, mostly related to a heavy aircraft and insufficient wind speeds. This results in a minimal cut-in wind speed for each system. However, instead of a gradual increasing from zero, the optimizer finds a feasible solution above cut-in wind speed with power closer to rated power (see  $A_{wing} = 80, 100 m^2$  in figure A5 or  $A_{wing} = 150 m^2$  in figure 12). Higher system mass does not seem to affect rated power,

400 which is determined by tether tension and tether speed constraints (i.e. no direct generator constraint). Only cut-in wind speed  
 No cut-out wind speed limitations were implemented. Therefore, wind power is only limited by each location's maximum wind  
 speed, which is significantly higher offshore (compare figure 2). All system sizes reach rated power at about  $U_{ref} = 10\text{ms}^{-1}$ ,  
 because the tether diameter of each AWES configuration was sized for this reference wind speed (see subsection 3.5). We  
 defined the same tether diameter for both onshore and offshore location. However, offshore AWES design could benefit from a  
 405 larger tether diameter as wind speeds are generally higher (see figure 2). This would result in higher rated power and a higher  
 AEP (see subsection 4.5). Higher lift coefficients result in higher rated power and a steeper power increase up to rated power.  
 Power variations are caused by local optima mostly occurring above rated wind speed as the system de-powers to stay within  
 tether force and flight speed constraints (see subsection 3.7).

In contrast to (Sommerfeld, 2020) the flight path length  $l_{path}$  (figure 12 second from top) remains almost constant with  
 410 wind speed. In comparison to this previous study overall path length is lower, which is probably due to the lower mass scaling  
 exponent of  $\kappa = 2.3$ . Path length increases with system size and mass due to higher inertia, longer tether length and an increased  
 minimal turning radius.



**Figure 12.** Power curve (top), path length (second from top), AWES power coefficient  $c_p^{AWES}$  (third from top) and AWES power coefficient divided by chord length  $c_p^{AWES}/c_{wing}$  (bottom) over reference wind speed  $100 \leq z \leq 400$  m for AWESs with  $A_{wing} = 10 - 150 \text{ m}^2$  and HL aerodynamic coefficients. Data is derived from p5, p50, p95 wind velocity profiles within each of the  $k = 10$  offshore clusters. Missing data points are the result of infeasible combination of optimization constraints and boundary conditions.

We estimate AWES power coefficients  $c_p^{AWES}$  to simplify the AWES power estimation and to compare AWES performance. We derive the power coefficient (see equation (6)) from the cycle average power  $\bar{P}$ , the swept area  $A_{swept}$  (wing span  $b_{wing}$

415 multiplied by path length  $l_{\text{path}}$ ) and reference wind speed  $U_{\text{ref}}$ , similar to conventional WTs. Since determining the wind speed  
along the flight path before deployment is impossible, we use average wind speeds between 100 m and 400 m as a proxy. The  
resulting trends shown in figure 12 (third from top) decrease non-linearly with wind speed, which can be attributed to different  
trajectories and increased losses associated with a longer tether, i.e. tether drag and weight. The AWES power coefficients  
seem to converge for wing areas larger than  $A_{\text{wing}} \geq 50 \text{ m}^2$ , while  $c_p^{\text{AWES}}$  of the smallest two aircraft sizes  $A_{\text{wing}} = 10, 20 \text{ m}$   
420 are significantly lower. A possible explanation is that smaller wings have a higher tether drag to lift force ratio, which might  
reduce the power coefficient. As expected, aerodynamic efficiency highly affects AWES power coefficients, with HL values  
almost doubling in comparison to the AP2 reference (compare figure 12 with A3 in the appendix).

Scaling the power coefficients with each system's wing chord  $c_{\text{wing}}$  collapses results onto a single curve (bottom). A possible  
explanation for this is that the mechanical power of a ground-generation AWES, which is the product of tether force and tether  
425 speed, scales with both wing area and path length. Path length increases with system size, but total cycle times remain almost  
constant, which results in an increased average flight speed (see subsection 4.1).

$$c_p^{\text{AWES}} = \frac{\bar{P}}{\frac{\rho_{\text{air}}}{2} A_{\text{swept}} U_{\text{ref}}^3} = \frac{\bar{P}}{\frac{\rho_{\text{air}}}{2} b_{\text{wing}} l_{\text{path}} U_{\text{ref}}^3} \quad (6)$$

**Markus: Make sure QSS figure is properly referenced, mention the dips in power in onshore power even with the QSS  
mdoel: must be due to wind profile shape!** This sub-section compares average power, annual energy production distribution  
430  $E$  and power harvest factor  $\zeta$  of optimized trajectories to the quasi steady-state model (QSS) described in sub-section 3.2.  
The top Sub-figures of figure 13 and 14 compare the effect of aerodynamic efficiency and location on cycle-average power for  
AWESs with a wing area of  $A_{\text{wing}} = 50 \text{ m}^2$  and a mass scaling exponent of  $\kappa = 2.7$ . The data are derived from 3 representative  
profiles from each of the 10 wind velocity clusters. Average wind speed between 100 and 400 m has been chosen as reference  
wind speed, because these are typical operating heights for these AWES. As of now, no standard reference wind speed  $U_{\text{ref}}$ ,  
435 equivalent to wind speed at hub height for conventional WT, has been agreed upon for AWES. Furthermore, using this altitude  
range results in comparable power curve trends onshore and offshore. Offshore AWES could benefit from a larger tether  
diameter as wind speeds are generally higher (see figure 2) which would result in higher rated power and a higher AEP. Higher  
lift coefficients result in higher rated power and a steeper power increase up to rated power. Power variations are caused by  
local optima mostly occurring above rated wind speed as the system de-powers to stay within tether force and flight speed  
440 constraints (see subsection 3.7)

Rated power, here defined as the maximum, almost constant average cycle power, which is constrained by instantaneous  
tether force and speed, is summarized in Table 4. Tether reel-in and reel-out are kept constant for all designs. No cut-out wind  
speed limitations were implemented. Therefore, wind power is only limited by each location's maximum wind speed, which is  
significantly higher offshore (compare figure 2). The table also shows the estimated equivalent WT rotor diameter  $D_{\text{WT}}^{\text{equiv}}$ , for  
445 an assumed power coefficient of  $c_p^{\text{WT}} = 0.4$  and a rated wind speed of  $10 \text{ ms}^{-1}$ . The system size and therefore material cost  
benefits of AWES become obvious when comparing AWES wing span  $b_{\text{wing}}$  to WT rotor diameter  $D_{\text{WT}}^{\text{equiv}}$ . AWES wing span  
is about 30 (HL) to 40 % (AP2) of the equivalent rotor diameter.

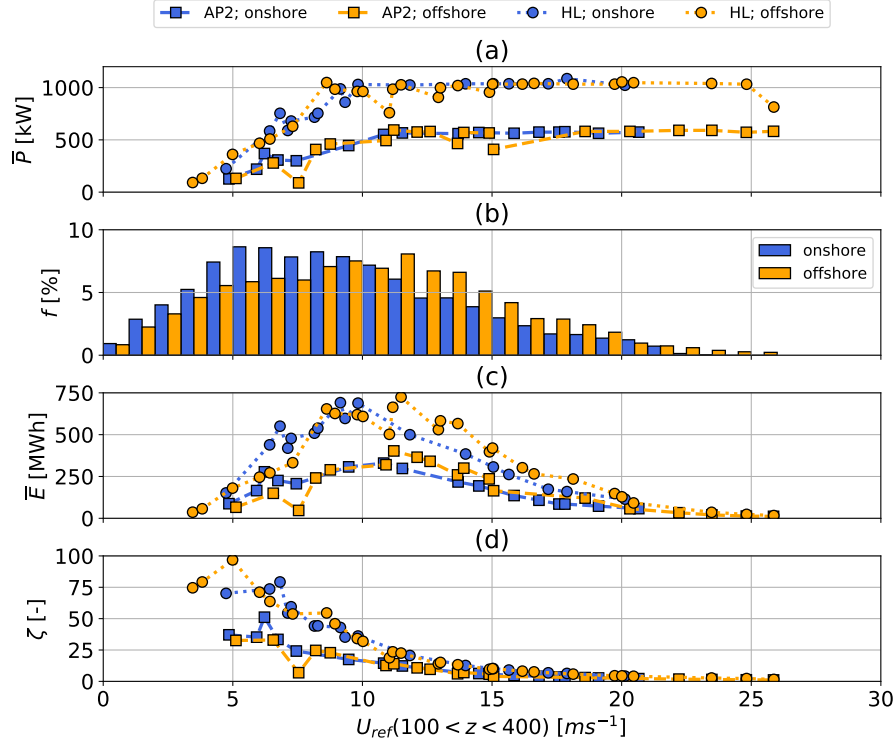


**Figure 13.** Representative AWES power curves (top) for both sets of HL (circle) and AP2 (square) reference aerodynamic coefficients for both onshore (blue) and offshore (orange) location. The masses of the  $A_{wing} = 50 \text{ m}^2$  wing area aircraft are scaled according to equation (4) with a mass exponent of  $\kappa = 2.7$ . Cycle-average power  $\bar{P}$  is derived from p5, p50, p95 wind velocity profiles within each of the  $k = 10$  WRF-simulated clusters. A reference height of  $100 \leq z_{ref} \leq 400 \text{ m}$  is used as a proxy for wind speed at operating altitude to calculate the annual wind speed probability distribution (center). The integral over the annual Energy production distribution (bottom) which is the product of power and wind speed probability distribution, yields the AEP (legend).

Tether diameter is adjusted according to aircraft area and aerodynamic efficiency so that all system sizes reach rated power at about  $U_{ref} = 10 \text{ ms}^{-1}$  (see subsection 3.5). Therefore, the HL configuration achieves higher rated power.  $AEP$  and  $cf$  almost  
450 doubles for HL in comparison to the AP2 reference, highlighting the importance of exploring high lift configurations. For comparison, tether diameter is kept constant for both locations. The QSS modeled power curves (see figure 14), which use the same wind profiles and tether diameter as the optimization model, achieve rated power at around  $U_{rated}(100 < z_{ref} < 400) \approx 8 \text{ ms}^{-1}$ . This is caused by the fact that the engineering model neglects mass and predicts optimal power production, whereas the dynamic optimization model resolves the flight trajectory and the varying forces and power within each production cycle. QSS onshore  
455 power deviates from offshore power, due to variation in wind conditions, despite always operating at optimal conditions.

The annual wind speed probability distribution  $f$  (b) represents the average annual wind speed between  $100 \leq z \leq 400 \text{ m}$  which stands in as a proxy for wind at operating altitude (see section 2). As expected, higher wind speeds are more likely to

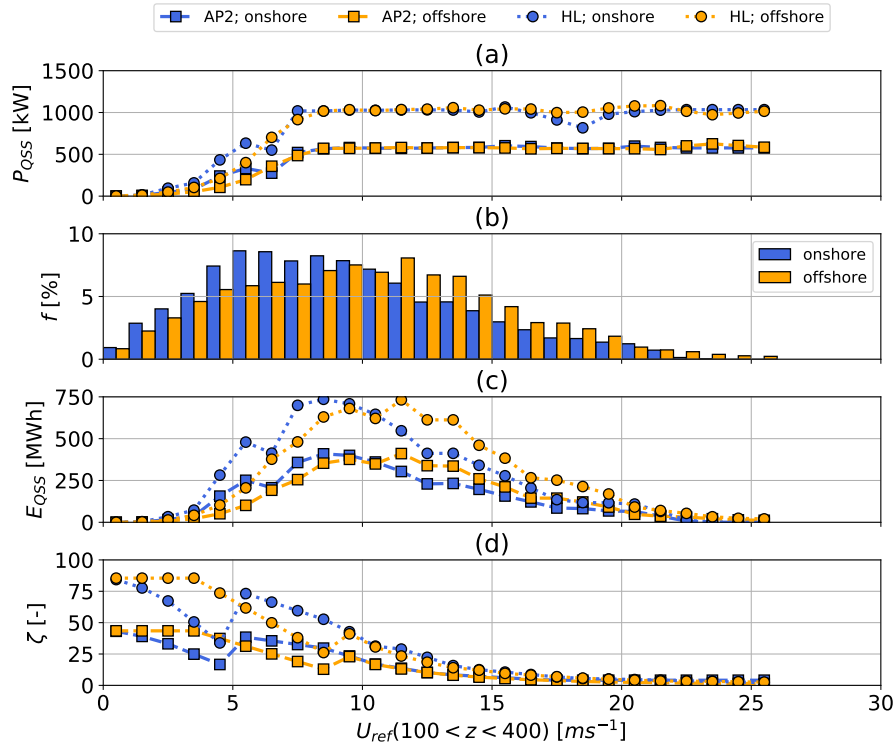


**Figure 14.** QSS model-based AWES power curves (top) for an AWES wing area of  $A_{\text{wing}} = 50 \text{ m}^2$ , both sets of HL (circle) and AP2 (square) reference aerodynamic coefficients and both onshore (blue) and offshore (orange) location. Optimal power  $\bar{P}_{\text{Lowd}}$  is derived from p5, p25, p50, p75, p95 wind speed profiles within each of the  $k=10$  WRF-simulated clusters. A reference height of  $100 < z_{\text{ref}} \leq 400 \text{ m}$  is used as a proxy for wind speed at operating altitude to calculate the annual wind speed probability distribution (center). The integral over the annual energy production distribution (bottom) which is the product of power and wind speed probability distribution, yields the AEP (legend)

**Table 4.** Rated power of AWES with a mass scaling exponent of  $\kappa = 2.7$  and equivalent wind turbine rotor diameter

$A_{\text{wing}} [\text{m}^2]$	10		20		50		80		100		150	
$b_{\text{wing}} [\text{m}]$	10		14.1		22.4		28.3		31.6		38.7	
aerodynamic coeff.	AP2	HL	AP2	HL	AP2	HL	AP2	HL	AP2	HL	AP2	HL
$\bar{P}_{\text{rated}} [\text{kW}]$	145	200	265	420	575	1030	1045	1800	1600	2225	2000	3400
$D_{\text{WT}}^{\text{equiv}} [\text{m}]$	27	32	37	47	55	73	74	97	91	108	102	132

460 occur offshore (FINO3) than onshore (Pritzwalk). However, very high wind speeds above  $U_{\text{ref}} > 18 - 20 \text{ ms}^{-1}$ , beyond the cut-off speed of realistic wind energy converters, have a very low chance occurrence at both locations. The resulting annual average energy production distributions  $\bar{E}$  (c) reveal a clear difference between the offshore and onshore energy potential. Better wind conditions offshore result in higher AEP and  $cf$  (sub-section 4.5).

Estimate energy production distributions  $E_{\text{QSS}}$ , AEP and cf (Figure 14) of the QSS reference model are based on the same wind speed distribution as the optimization model. The QSS model predicts a higher energy production distribution (c) up to rated wind speed than the optimization model, because of the lack of a defined cut-in wind speed and a sooner rated power. Beyond rated power,  $E_{\text{QSS}}$  is similar to optimized results, as predicted power is very similar, except some small variation. This leads to a higher AEP and cf predictions (Figure 17).

Sub-figure (d) in figures 13 and 14 presents the power harvest factor  $\zeta$  Diehl (2013), which sets optimal AWES power  $P_{\text{opt}}$  in relation to the total wind power of a cross sectional area of the same size as a given wing  $A_{\text{wing}}$ .

$$\zeta = \frac{P}{P_{\text{area}}} = \frac{P_{\text{opt}}}{\frac{1}{2}\rho_{\text{air}}A_{\text{wing}}U(z)^3} \leq \frac{4}{27}c_{\text{R}} \left( \frac{c_{\text{R}}}{c_{\text{D}}} \right)^2 \quad (7)$$

$U(z)$  is the wind speed and  $\rho_{\text{air}}(z)$  the air density at operating altitude. The power harvest factor decreases steadily for both the optimization and QSS model. The QSS model predicts an almost constant  $\zeta$  at low wind speeds ( $U_{\text{ref}} < 5 \text{ ms}^{-1}$ ).  
**Markus: double check power and zeta calculation for QSS. why a drop in zeta onshore even though power increases?**  
**From Thesis: because  $\alpha$  is set to maximize  $c_{\text{R}}^3/c_{\text{D},\text{total}}^2$  and tether length remains constant.**

#### 4.5 AEP Annual energy production and capacity factor

We estimate the annual energy production (AEP) and capacity factor (cf) (equation (8)) from the previously described power curve  $\bar{P}$  (subsection 4.4) and annual wind speed probability distribution  $f$ , derived from the histogram of annual wind speeds seen in the bottom subfigure of figure 2. Rated power  $P_{\text{rated}}$  is defined from optimization results, as the a priori estimation of nonlinear, trajectory dependent losses is difficult.

**Markus: read again and fix. moved paragraphs. Furthermore, offshore AEP always outperforms onshore AEP the QSS model.** The previously described power curves  $\bar{P}$  (a) and annual wind speed probability distributions  $f$  (b) allow the investigation of the annual energy production distribution  $E$  (c) and therefore annual energy production (AEP) as well as capacity factor (cf):

$$\text{AEP} = \sum_{i=1}^k (\bar{P}_i f_i) 8760 \frac{\text{h}}{\text{year}} \quad \text{cf} = \frac{\text{AEP}}{P_{\text{rated}}} \quad (8)$$

Figure 13 compares the impact of aerodynamic efficiency by contrasting the previously described power curve (top) for AWESs with a wing area of  $A_{\text{wing}} = 50 \text{ m}^2$  and a mass scaling exponent of  $\kappa = 2.7$ . Data for high lift aerodynamic coefficients are highlighted by a circle while AP2 reference data is marked by a square. Wind conditions are the p5, p50, p95 percentile onshore (blue) and offshore (orange) wind velocity profiles for each of the  $k = 10$  clusters. The center sub-figure summarizes the wind speed probability distribution between  $100 \leq z \leq 400 \text{ m}$  which stands in as a proxy for wind at operating altitude (see section 2). As expected, higher wind speeds are more likely to occur offshore (FINO3) than onshore (Pritzwalk). However, very high wind speeds above  $U_{\text{ref}} > 18 - 20 \text{ ms}^{-1}$ , beyond the cut-off speed of realistic wind energy converters, have a very low

chance occurrence at both locations. The resulting annual average energy production distributions  $\bar{E}$  (bottom) reveal a clear difference between the offshore and onshore energy potential. Better wind conditions offshore lead result in higher  $AEP$  and  $cf$ . Higher aerodynamic efficiency increases rated power and power up to rated wind speed. Therefore,  $AEP$  and  $cf$  almost doubles for HL in comparison to the AP2 reference, highlighting the importance of exploring high lift configurations.

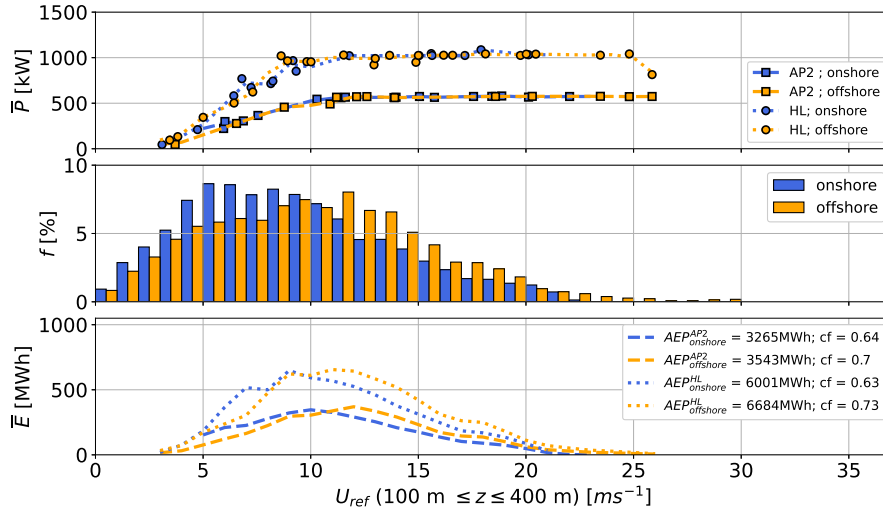


**Figure 15.** Representative AWES power curves (top) for both sets of HL (circle) and AP2 (square) reference aerodynamic coefficients for both onshore (blue) and offshore (orange) location. The masses of the  $A_{\text{wing}} = 50 \text{ m}^2$  wing area aircraft are scaled according to equation (4) with a mass exponent of  $\kappa = 2.7$ . Cycle-average power  $\bar{P}$  is derived from p5, p50, p95 wind velocity profiles within each of the  $k = 10$  WRF-simulated clusters. A reference height of  $100 \leq z_{\text{ref}} \leq 400 \text{ m}$  is used as a proxy for wind speed at operating altitude to calculate the annual wind speed probability distribution (center). The integral over the annual energy production distribution (bottom) which is the product of power and wind speed probability distribution, yields the AEP (legend).

495 Figure 17 compares the  $AEP$  and  $cf$  estimates for all system sizes scaled with a mass scaling exponent of  $\kappa = 2.7$ . The left side of figure 17 compares onshore AEP (a,b) and  $cf$  (c,d) for all system sizes scaled with a mass scaling exponent of  $\kappa = 2.7$  to QSS data, while the right side compares offshore results. AEP increases almost linearly with wing area  $A_{\text{wing}}$ , because power, which is the product of tether force and tether speed, scales with wing area. Tether force scales linearly with wing area and maximum tether speed is kept constant throughout all optimization runs. As expected HL aerodynamic coefficients (circle) outperform the AP2 reference (square). Offshore (orange) AEP and  $cf$  is generally higher than onshore (blue) because of the higher likelihood of higher wind speeds. The QSS model predicts higher AEP, because of the previously described differences in power up to rated wind speed, but follows the same trends. The optimization model predicts lower average AEP at  $A_{\text{wing}} = 150 \text{ m}^2$ , due to the high number of infeasible solutions at lower wind speeds, equivalent to not being able to fly due to weight (see figure 12). Overall  $cf$  (bottom) (c,d) remains almost unchanged for wing sizes up to  $A_{\text{wing}} = 100 \text{ m}^2$  and sharply declines for  $A_{\text{wing}} = 150 \text{ m}^2$ . , due to the high number of infeasible solutions at lower wind speeds, equivalent to not

500

505

being able to fly due to weight (see figure 12). The QSS model predicts very high  $cf$  values at both locations. Markus: why drop at A 100 AP2?? MUST be def of prated?! The relatively high  $cf$  values are caused by the the result of relatively low rated wind speed of  $U_{\text{rated}} = 10 \text{ ms}^{-1}$ . This leads to a design trade-off between generator size relative to wing area and tether diameter, similar to conventional WT. Onshore AEP and  $cf$  seems to outperform offshore for wing areas larger than  $100 \text{ m}^2$ .

510 This is likely caused by outliers, or wind velocity profile specific local minima, in the power curve (compare to power curve figure A7 in appendix) before rated wind speed ( $v_{\text{rated}} = 10 \text{ ms}^{-1}$ ), where the system seemingly over-performs. Furthermore, offshore AEP always outperforms onshore AEP in the QSS model.

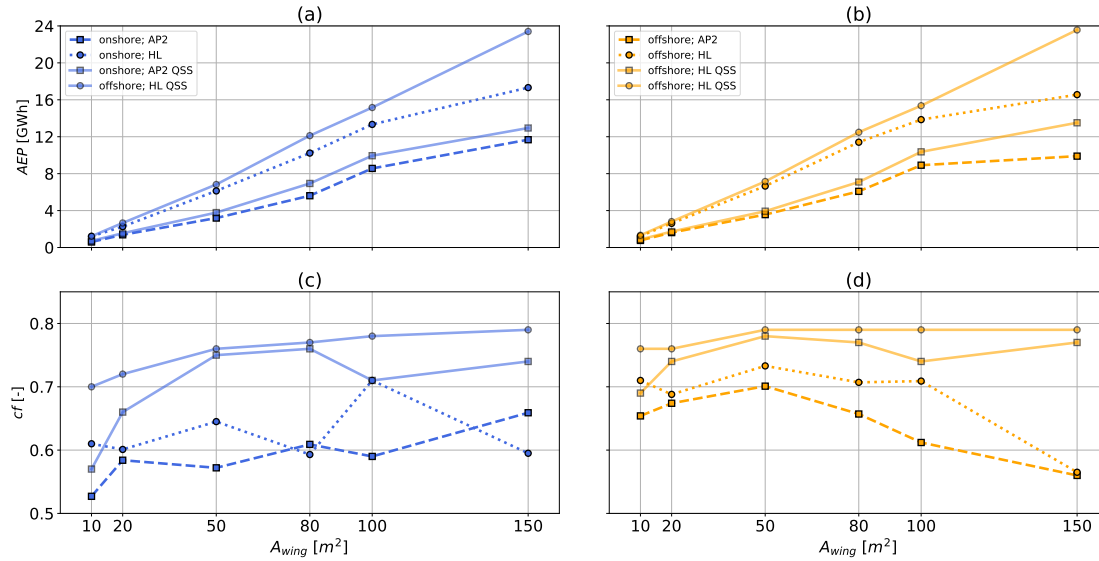


**Figure 16.** Representative AWES AEP (a,b) and  $cf$  (c,d) over aircraft wing area  $A_{\text{wing}}$  scaled according to equation (4) with a mass exponent of  $\kappa = 2.7$ . QSS model (solid lines) results are included for reference (sub-section 3.2). These figures summarize data for both sets of HL (circle) and AP2 (square) aerodynamic coefficients as well as both onshore (left, blue) and offshore (right, orange) location. Results are based on the cycle-average power  $\bar{P}$  derived from p5, p50, p95 wind velocity profiles within each of the  $k = 10$  WRF-simulated clusters and wind speed probability distribution between  $100 \leq z_{\text{ref}} \leq 400 \text{ m}$ , used as a proxy for wind speed at operating height.

Figure 18 compares AEP for a mass scaling exponents of  $\kappa = 2.7$  to scaling with  $\kappa = 3$  and  $\kappa = 3.3$ , both onshore and offshore. Heavy configurations with no feasible trajectory at any wind speed result in missing data. While smaller systems seem almost unaffected by aircraft weight, mass scaling effects lead to significant reduction in AEP for larger AWES. This is particularly true for wings with aerodynamic reference coefficients (AP2, square) and onshore wind conditions. Combining results from both figure 17, which already shows diminishing returns in AEP and  $cf$  with increasing wing area for the lightest, idealized aircraft mass scaling, and figure 18, which predicts that AEP will only decline for heavier mass scaling, conveys that upscaling AWES is only beneficial with significant weight reduction. These results hint at the existence of an upper limit of

515

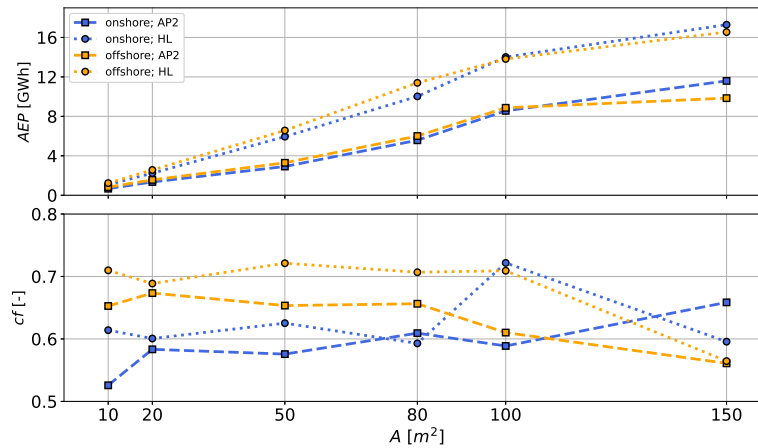


**Figure 17.** Representative AWES AEP (top) and cf (bottom) over aircraft wing area  $A_{\text{wing}}$  scaled according to equation (4) with a mass exponent of  $\kappa = 2.7$ . Figure summarizes data for both sets of HL (circle) and AP2 (square) reference aerodynamic coefficients as well as both onshore (blue) and offshore (orange) location. Results are based on the cycle-average power  $\bar{P}$  derived from p5, p50, p95 wind velocity profiles within each of the  $k = 10$  WRF-simulated clusters and wind speed probability distribution between  $100 \leq z_{\text{ref}} \leq 400$  m, used as a proxy for wind speed at operating height.

520 AWES weight relative to AWES size or lift (see subsection 4.6), which is plausible since mass scales with aircraft volume and lift scales with aircraft area. Therefore and for compensating power fluctuation caused by the cyclic nature of ground-generation AWES, it is likely better to deploy multiple smaller scale devices rather than a single large-scale system. **Determining** The ideal, site-specific AWES size needs to be determined by realistic mass scaling and the local wind resource.

#### 4.6 Impact of weight and drag

525 The most effective AWES concept benefit from increased apparent wind speed during crosswind flight (Loyd, 1980), such as the ground-generation concept investigated in this study. Such trajectories, whether circular or figure-of-eight, always include an ascent during each loop where the aircraft needs to overcome gravity to gain altitude. This leads to a deceleration and therefore reduction of aerodynamic lift. AWESs with excess mass fail to overcome weight and drag and can no longer climb.

With an increased wing area, the entire aircraft, particularly the load carrying structures such as the wing box, need to increase in size and weight in order to withstand increased aerodynamic loads produced by a larger wing. Aircraft mass scales with volume ( $\kappa = 3$ ), assuming pure geometric scaling without design improvements, while lift force and therefore power only scales with the area ( $F_{\text{lift}} \sim b^2$ ). However, when tether drag is considered AWES power scales faster than  $b^2$ , because tether drag losses are proportional to the tether diameter, which scales relative to the square root of the wing area. Similarly, conventional WT power and AEP scales with the rotor diameter square, while theoretic WT mass scales with the cube of the rotor diameter. However, comparing both wind energy converters under these assumptions, AWES perform worse as their flight

535

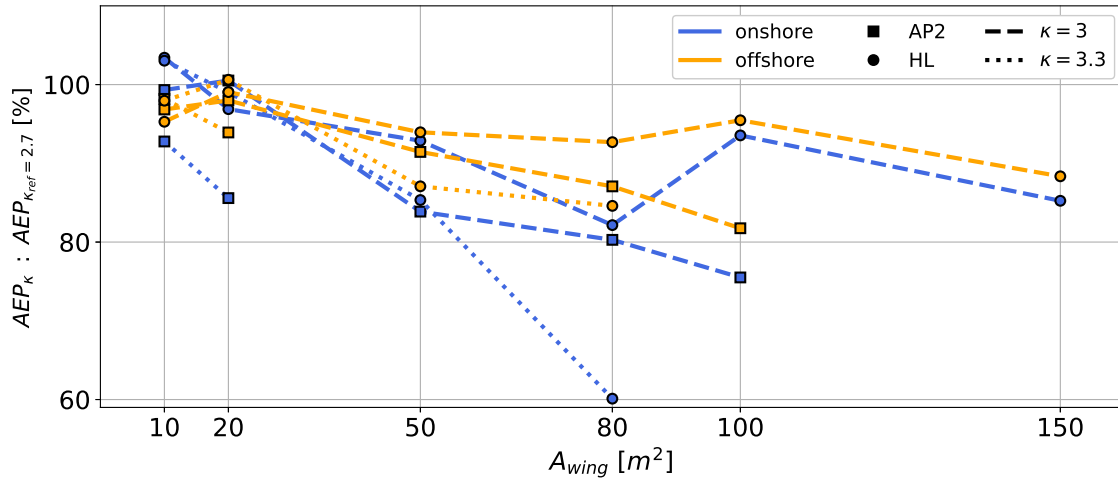


**Figure 18.** AEP ratio for mass scaling exponent  $\kappa = 3$  (dashed lines) and  $\kappa = 3.3$  (dotted lines) relative to AEP of  $\kappa = 2.7$  over aircraft wing area  $A_{wing}$ . Figure summarizes data for both onshore (blue) and offshore (orange) location as well as both sets aerodynamic coefficients HL (circle) and AP2 (square). Results are based on the cycle-average power  $\bar{P}$  derived from p5, p50, p95 wind velocity profiles within each of the  $k = 10$  WRF-simulated clusters. Missing data points indicate that no feasible solution for any wind velocity profile was found.

path degrades. This can be attributed to the fact that AWES need to produce enough lift to carry their own weight to maintain operational, while WT are supported by a tower.

These facts limit AWES size, as the prevailing wind resource does not improve enough to produce sufficient aerodynamic lift to overcome the increased system drag and weight. An increase of operating altitude only comes with a marginal wind speed increase especially offshore (compare figure 2). Furthermore, higher operating altitudes also lead to increased cosine losses, unless offset by a longer tether which in turn results in more drag and weight. Better aerodynamics or lighter, more durable aircraft and tether materials can only push this boundary, but not overcome it.

A comparison of tether weight  $W_{tether}$  during the production phase (reel-out) to total system weight ( $W_{total} = W_{aircraft} + W_{tether}$ ) in figure 19 (top) shows that the tether makes up 10 to 30 % of the entire system weight. Note that the tether cross sectional area is sized with a safety factor of 3. Tether cross sectional area mostly scales with aerodynamic force and therefore wing area while the aircraft weight scales with a mass scaling exponent  $\kappa > 2.7, 3.0$  which results in decreasing trend lines. This value is higher for high lift airfoils (circle) as the tether diameter is larger to withstand higher aerodynamic forces. For lighter aircraft, scaled with  $\kappa = 2.7$  (dash-dotted), the portion of tether weight is higher because the tether diameter remains constant while the aircraft mass is lighter.

The bottom sub-figure reveals that tether drag makes up about 15 to 40 % of the entire system drag during the production phase. Tether diameter  $d_{tether}$  and therefore face area ( $A_{tether}^{face} = d_{tether} l_{tether}$ ) scales beneficially with wing area, leading to the downward trend lines. **For this evaluation half the simulated tether drag is attributed to the aircraft and the other half to the ground station.** As described in Sub-section 3.5, the total tether drag is divided up evenly between the top and bottom node at

every tether segment, resulting in half the tether drag being attributed to the aircraft and the other half to the ground station.

555 Implementing more detailed tether models could explore the impact of tether dynamics and tether drag in more detail.

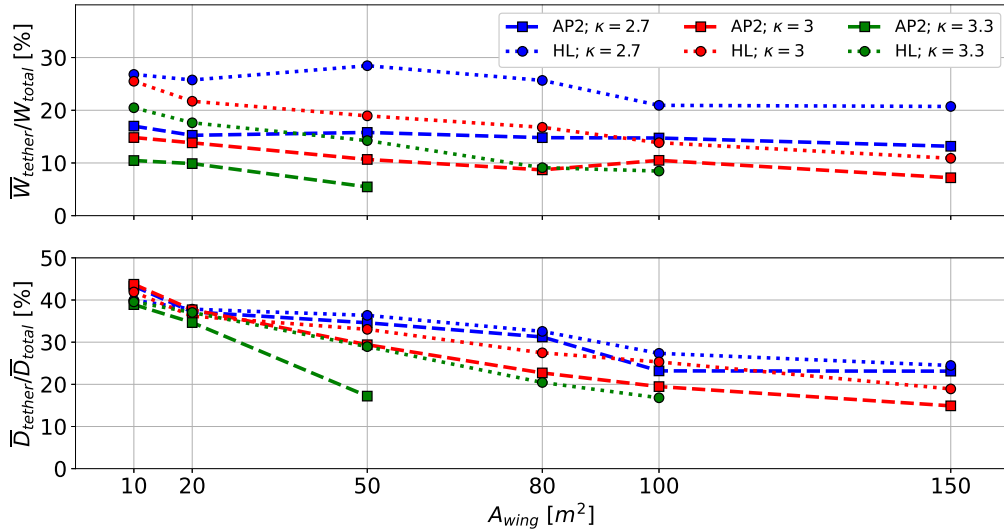


**Figure 19.** Percentage of cycle-average tether weight  $\bar{W}_{tether}$  to total weight  $\bar{W}_{total}$  (top) and tether drag  $\bar{D}_{tether}$  to total drag  $\bar{D}_{total}$  (bottom) during production phase (reel-out) for all aircraft sizes  $A_{wing} = 10 - 150 m^2$ , sets of aerodynamic coefficients AP2, HL and mass scaling exponents  $\kappa = 2.7, 3, 3.3$  for wind data at the offshore location.

It is critical for crosswind AWES to ascend during each loop of the production or reel-out phase. The aircraft needs to produce enough aerodynamic lift, which decreases as the aircraft slows down during ascent (compare 7), to overcome gravity. During the ascent, the aircraft increases angle of attack (figure 8) to compensate for the decreased apparent wind speed. However, this is not enough to maintain aerodynamic force and tether tension during times of lower wind speeds, especially for larger and heavier systems.

560 The top sub-figure in figure 20 contrasts the aeronautic load factor defined as the ratio of average lift force  $\bar{L}_{wing}$  to total AWES weight  $\bar{W}_{total}$ , including tether with a safety factor of 3 and aircraft, during the reel-out phase for all aircraft sizes  $A_{wing} = 10 - 150m^2$ , mass scaling exponents  $\kappa = 2.7, 3.0, 3.3$  and aerodynamic coefficients HL, AP2. The average load factor decreases from about 10 - 20 to 10 - 5, depending on aerodynamic performance and mass scaling, which is approximately the maneuvering load factor of an acrobatic airplane  $n_{acrobatic} = 6.0$  (Federal Aviation Agency, 2017). For

565 utility airplanes this value is about  $n_{acrobatic} = 4.4$ . The beneficial effect of better aerodynamics and mass scaling are clearly visible in a lower weight to lift ratio. High system mass with insufficient lift on the other hand leads to infeasible solutions and missing data.

The bottom sub-figure of figure 20 shows a slight reduction of total average drag  $\bar{D}_{total}$  to average lift  $\bar{L}_{wing}$  ratio with increasing wing area. Overall however, this ratio remains almost constant between 6 to 8 %. The increase for  $A_{wing} =$

570 100, 150  $m^2$ ,  $\kappa = 3$  and AP2 aerodynamics is likely caused by local optimization minima and few feasible wind speed pro-

files. For this investigation half the tether drag is assigned to aircraft and the other half to ground station. Markus: Add a comparison to L/D using 3 Ref1: Did you use the tether drag in consistent way with literature for the evaluation of the system glide ratio? equation 4.8 in Efficiency of Traction Power Conversion Based on Crosswind Motion", Ivan Argatov and Risto Silvennoinen in "Airborne Wind Energy", Ahrens, Diehl, Schmehl (2013). Using the mentioned equation can be a simple check for your results

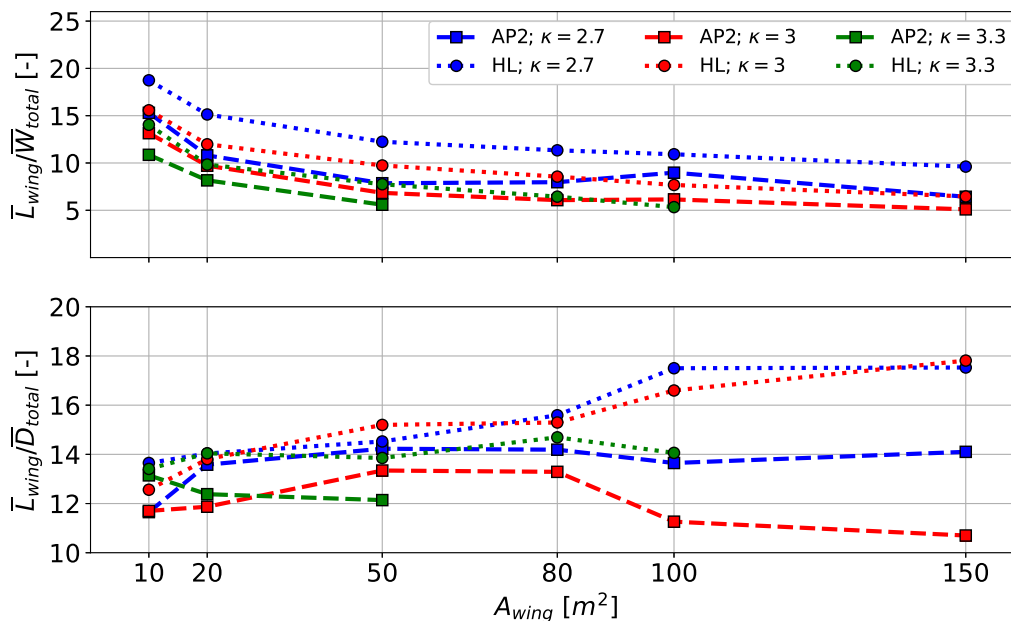


**Figure 20.** Load factor or lift  $\bar{L}_{wing}$  to  $\bar{W}_{total}$  ratio (top) and cycle-average total lift  $\bar{L}_{wing}$  to drag  $\bar{D}_{total}$ , including tether drag, (bottom) during production phase (reel-out) for all aircraft sizes  $A_{wing} = 10 - 150 m^2$ , sets of aerodynamic coefficients AP2, HL and mass scaling exponents  $\kappa = 2.7, 3, 3.3$  for wind data at the offshore location. Large-scale results for  $A_{wing} = 100, 150 m^2$  might be misleading because only high wind speeds result in feasible solutions (compare figures 21 and A9).

For a large-scale aircraft with an area of  $A_{wing} = 150 m^2$ , scaled with the lightest mass scaling exponent of  $\kappa = 2.7$ , and AP2 reference aerodynamic coefficients, no feasible solution could be found for low wind speeds  $U_{ref} < 5ms^{-1}$ . This can be seen in figure 21 which shows the total weight  $\bar{W}_{total}$ , including tether and aircraft, divided by average lift  $\bar{L}_{wing}$  for all aircraft sizes with AP2 reference aerodynamic scaled with  $\kappa = 2.7$  (compare to data derived from HL aerodynamic coefficients and  $\kappa = 3.0$  in figure A9 in the appendix). Weight to lift ratio decreases up to  $U_{ref} \approx 5ms^{-1}$ , above which it remains almost constant. This can likely be attributed to the applied apparent flight speed constraint of  $U_{app}^{max} = 80ms^{-1}$  which seems to already be achieved at this reference wind speed. These data suggest that the minimum viable load factor is about 5 (equivalent to a maximum viable weight to lift ratio of 20 %) for the given design and flight speed constraints. ref2:Please add additional data to back

**this hypothesis. Would this change if the cycle time changes? This seems again an artefact of the model implementation, and not a physical effect. If this is not the case, please motivate.**

585

The bottom subfigure of figure 21 shows the total AWES drag  $\bar{D}_{total}$ , including tether drag, to lift ratio  $\bar{L}_{wing}$  over reference wind speed for all aircraft sizes scaled with  $\kappa = 2.7$  and AP2 reference aerodynamic coefficients. Data for all aircraft sizes show a similar trend with the drag proportion doubling from about 5 to 10 % with wind speed. This increase is primarily caused by longer tether lengths at higher wind speeds (compare figure 10), which results in more drag and weight. Heavier system weight also leads to an angle of attack  $\alpha$  increase as the aircraft needs to produce more lift while staying within the flight speed constraint.

590

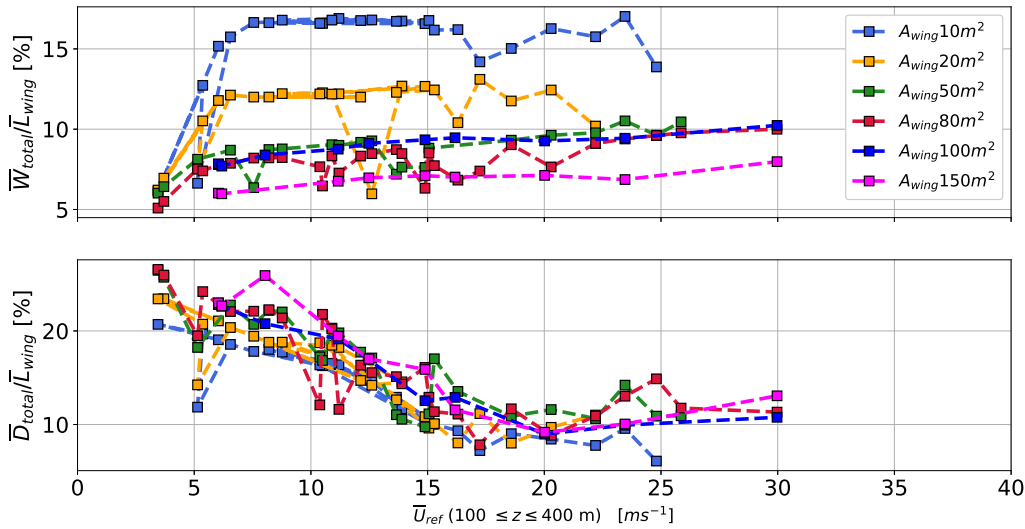


**Figure 21.** Ratio of cycle-average total weight  $\bar{W}_{total}$  to lift  $\bar{L}_{wing}$  (top) and cycle-average total drag  $\bar{D}_{total}$ , including tether drag, to lift  $\bar{L}_{wing}$  (bottom) during production phase (reel-out) for all aircraft sizes  $A_{wing} = 10 - 150 m^2$  for AP2 reference aerodynamic coefficients and a mass scaling exponent of  $\kappa = 2.7$  over reference wind speed offshore.

#### 4.7 Power losses

Increased aircraft wing area not only leads to increased power potential, but is also accompanied by increased tether losses due to weight and drag. Tether mass scales with aircraft wing size because the higher aerodynamic forces require a larger tether diameter, assuming constant tether strength. Tether length increases with AWES size and wind speed (see subsection 4.2) which further increases tether drag and weight.

595

Figure 22 compares the average tether power losses  $\bar{P}_{tether}^{drag}$ , [calculated from the tether drag assigned to the aircraft node and its flight speed](#), relative to average cycle power  $\bar{P}$  for all aircraft wing sizes  $A_{wing} = 10 - 150 m^2$ , mass scaling exponents

$\kappa = 2.7, 3.0, 3.3$  and both sets of aerodynamic coefficients (HL, AP2). [This power loss can be interpreted as how much of the harvested wind power is dissipated by the tether.](#) The relative tether drag loss decreases with wing area, because tether diameter scales beneficially with the square root of the tether force which scales linearly with wing area. This scaling trend is encouraging, but is counteracted and dominated by mass increases with size highlighted in earlier sections. As expected, the high lift airfoil HL (dotted lines) experiences less relative drag loss than the AP2 reference airfoil (dashed lines) due to higher average cycle power.

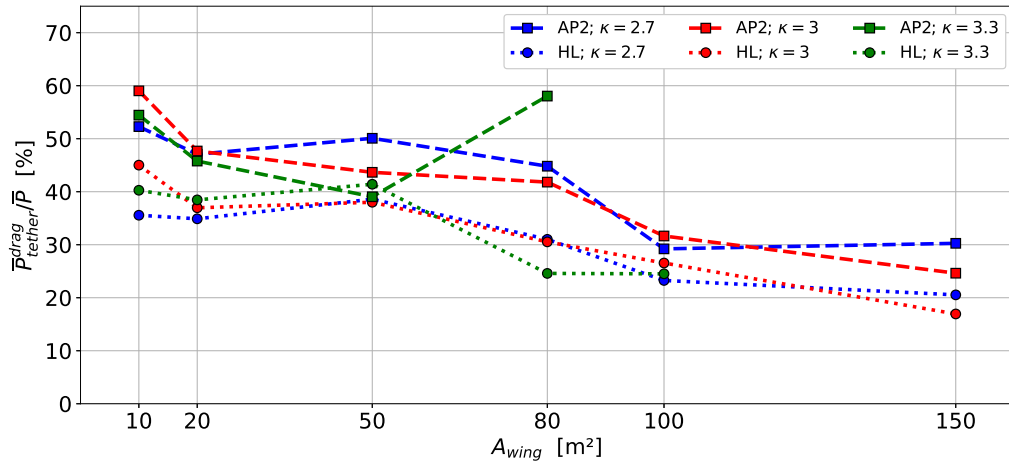


**Figure 22.** Ratio of cycle-average power losses due to tether drag  $\bar{P}_{tether}^{drag}$  to produced power  $\bar{P}$  over aircraft size  $A_{wing}$  for both sets of aerodynamic coefficients AP2, HL, all mass scaling exponent of  $\kappa = 2.7, 3.0, 3.3$  and wind data at the offshore location.

## 605 5 Summary and conclusion

This study presents AWES scaling trends and explores the AWES design space subject to representative onshore (Pritzwalk in northern Germany) and offshore (FINO3 research platform in the North Sea) wind conditions. [Tether speed range and tether diameter of every design \(size and aerodynamic coefficients\) were fixed. This can be interpreted as generator limitations on speed, torque and power which result in a constant maximum AWES power and a power curve as a function of wind speed.](#)

610 We evaluate the impact of wing area and mass scaling as well as nonlinear aerodynamic properties on optimal trajectories, reaction forces and moments, power generation and AEP, based on the `awebox` power and trajectory optimization model. Our analyses estimate a maximum average weight to average lift ratio (equivalent to a load factor of about 5) to allow viable AWES operation of about 20 %. Our results imply the existence of an upper limit of AWES weight relative to AWES size or lift, which is plausible since mass scales with aircraft volume and lift scales with aircraft area. In comparison, conventional WT  
615 power scales with the square and mass with the cube of the rotor diameter. Under the same assumptions AWES performance scales worse because the aircraft needs to carry ~~its own~~ [the entire](#) increasing [system](#) weight ([including tether mass](#)), instead of being supported by a tower. Therefore, the optimal AWES size is always defined by the maximum weight which the aircraft can support, subject to local wind conditions.

In this work we described and analyzed ground-generation AWES scaling effects subject to realistic wind velocity profiles  
620 for a set of representative AWES. We compare the impact of several design parameters based on the Ampyx AP2 reference model. We analyze AWES performance for two sets of nonlinear aerodynamic coefficients, the AP2 reference and [a high lift configuration where AP2 coefficients were adjusted as if high lift devices were attached](#) ~~-wing with high lift airfoil~~. To assess AWES scaling potential, several wing areas between  $A_{\text{wing}} = 10 - 150$  m, with mass properties scaled according to a geometric scaling law with three different mass scaling exponents  $\kappa = 2.7, 3.0, 3.3$ , were implemented into the `awebox` power  
625 and trajectory optimization toolbox. A representative set of k-means clustered onshore and offshore wind velocity profiles, derived from the mesoscale WRF model, were used to define wind inflow conditions.

We discussed the impact of mass and system size on typical trajectories and time series data which confirms that instantaneous power can drop to zero during the reel-out phase. This is caused by insufficient lift as the aircraft tries to overcome gravity and maintain tether tension. The minimum wind speed to sustain positive power production during the reel-out phase as  
630 well as tether length and average operating altitude increase with system size and weight. However, operating heights beyond 500 m are rare and mostly occur as the system de-powers above rated wind speed to stay within tether force and flight speed constraints. [Therefore, it could be reasonable to keep the maximum tether length and operating altitude below those values to reduce costs and permitting burdens.](#) As these constraints become active, the resulting trajectory deforms and diverge from the expected paths seen for lower wind speeds. This is especially true for high lift [airfoils configurations](#) as they reach these limits  
635 faster. er losses, Since detailed design and stress analysis is beyond the scope of this paper, we limit ourselves to the estimation of maximum mechanical wing loads, assuming [an](#) elliptical lift distribution. Shear force scales linearly with wing area, while bending moment increases nonlinearly with wing area and wing span.

Analyzing the AWES power curve we determine that rated power scales linearly with wing area, assuming that tether speed constraint are kept constant and the tether diameter is adjusted appropriately. We chose to size the tether diameter so that rated power is achieved at about  $U_{\text{ref}} = 10\text{ms}^{-1}$ , independent of size, mass and location. A larger tether diameter would increase rated power and shift rated speed towards higher wind speeds, which might be beneficial for faster offshore wind conditions, but would impact tether drag and weight. Improving aerodynamic efficiency increases power production. For the sets of aerodynamic coefficients used in this study, average power increased by approximately 30% to 80 %, depending on wing area. We proposed the nonlinear AWES power coefficient  $c_p^{\text{AWES}} c_{\text{wing}}^{-1}$  from the aircraft path length and wing area to collapse power curves.

We estimate AEP and cf based on the power curve analysis and wind speed probability distribution at reference height between  $100 \leq z_{\text{ref}} \leq 400$  m. Offshore AEP is generally higher than onshore, while the power curves are almost identical even though clustered profiles differ, due to higher wind speeds. Increased aircraft mass leads to significant reduction in AEP, as lower wind speeds become infeasible to fly in until finally no feasible solutions, even at higher wind speeds, can be found. This is particularly true for the onshore location and AP2 reference aerodynamics, as these conditions do can not produce sufficient lift force to overcome system weight. Wind farm setups might therefore benefit from the deployment of multiple smaller AWES rather than few large-scale AWES. This could also reduce the overall power loss when synchronizing the flight trajectories of AWESs within a farm. Determining the ideal, site-specific AWES size needs to be determined subject to realistic mass scaling, the available area and the local wind resource.

Furthermore, we describe the tether contribution to total weight and drag relative to aircraft wing size as well as tether-associated power losses. Our results show that even though relative tether power losses decrease with wing size, they still use up a significant portion (20 - 60 %) of the average mechanical AWES power.

Lastly, we try to determine the maximum AWES weight to lift ratio. Our data shows that total AWES weight, including tether and aircraft, should not exceed 20 % of the produced aerodynamic lift to operate. The limitation of crosswind AWES operations seems to be the upward climb within each loop. During this ascent the aircraft decelerates by approximately 20%-25%, which reduces aerodynamic lift by about 35% - 45%, which could be offset by the deployment of additional high-lift devices. As a result the system can not produce enough lift to overcome gravity and maintain tether tension, leading to a reduction in tether speed and produced power up until a complete drop to zero for lower wind speeds.

## 6 Future work

Defining the AWES design space subject to realistic wind conditions and operating constraints is crucial for scaling this technology for large-scale deployment of grid-integration. We therefore propose to build upon this study and further investigate the design space using design optimization. A possible approach is to utilize the already existing AWES power and trajectory optimization toolbox `awebox` and implement it into a design optimization framework that varies parameters such as aspect ratio, wing area and wing box dimensions. Adding a cost model would allow to optimize for levelized cost of electricity [or](#) [AEP](#). Analyzing the dynamic aircraft wing loads caused by the cyclic nature of crosswind AWES and turbulence could improve

AWES durability and further explore AWES design by considering fatigue loads to explore wing concepts to minimize  $\kappa$ . Ultimately, AWES must compete with conventional wind. Scaling and moving offshore are logical goals for both technologies. The relative merits of large-scale AWES must be further explored to set design and development targets, particularly since this study highlighted that offshore AWES are not particularly beneficial relative to conventional wind, given the generally lower shear offshore. [This further highlights that the advantage of ground-generation AWES, in particularly offshore, does not lie in higher altitudes, but in reduced material and associated benefits such as easier transportation.](#)

*Code availability.* TEXT

*Data availability.* TEXT

*Author contributions.* Markus Sommerfeld evaluated the data and wrote the manuscript in consultation and under the supervision of Curran  
680 Crawford. Martin Dörenkämper set up the numerical offshore simulation, contributed to the meteorological evaluation of the data. Jochem  
De Schutter co-developed the optimization model and helped writing and reviewed this manuscript.

*Competing interests.* We declare that neither the author nor any co-author can identify any conflict of interest regarding the subject matter  
or materials discussed in this manuscript.

*Acknowledgements.* The authors thank the BMWi for funding of the “OnKites I” and “OnKites II” project [grant number 0325394A] on the  
685 basis of a decision by the German Bundestag and project management Projektträger Jülich. We thank the PICS, NSERC and the DAAD for  
their funding.

`awebbox` has been developed in collaboration with the company Kiteswarms Ltd. The company has also supported the `awebbox` project  
through research funding. The `awebbox` project has received funding from the European Union’s Horizon 2020 research and innovation  
program under the Marie Skłodowska-Curie grant agreement No 642682 (AWESCO)

690 We thank the Carl von Ossietzky University of Oldenburg and the Energy Meteorology research group for providing access to their High  
Performance Computing cluster *EDDY* and ongoing support.

We further acknowledge Rachel Leuthold (University of Freiburg, SYSCOP) and Thilo Bronnenmeyer (Kiteswarms Ltd.) for their helped  
in writing this article and great technical `awebbox` support.

## Appendix A: figures

### 695 A1 Trajectory

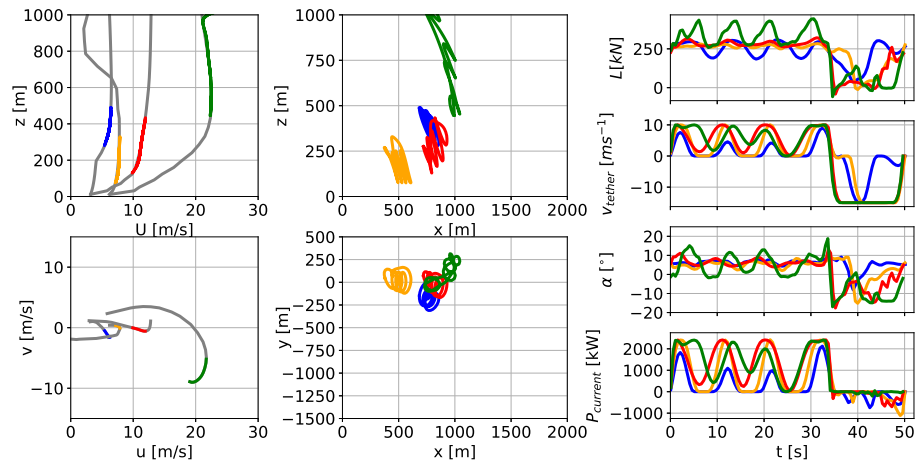


Figure A1. ap2-scaled-offshore

A2 Operating altitude

A3 power curves

A4 AEP

A5 weight and drag to lift

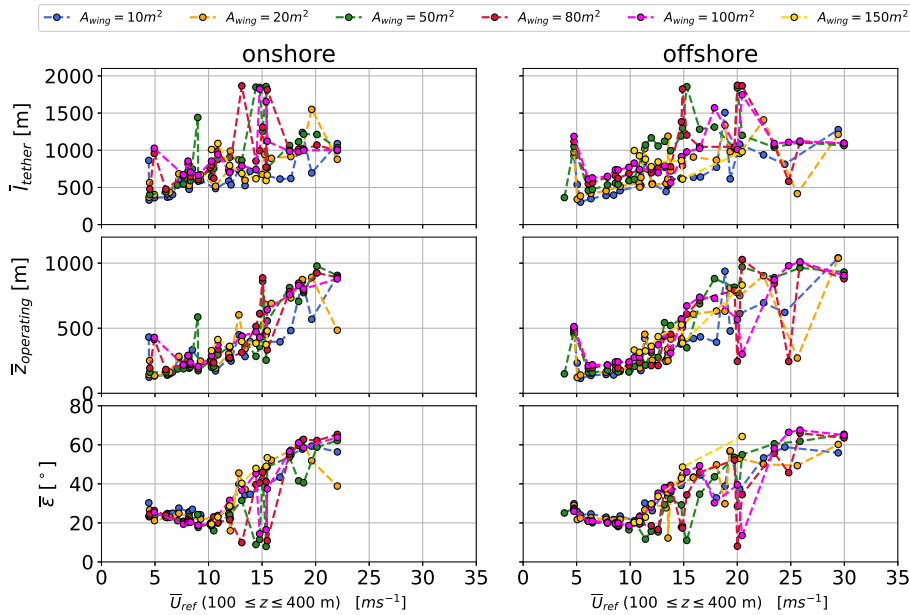
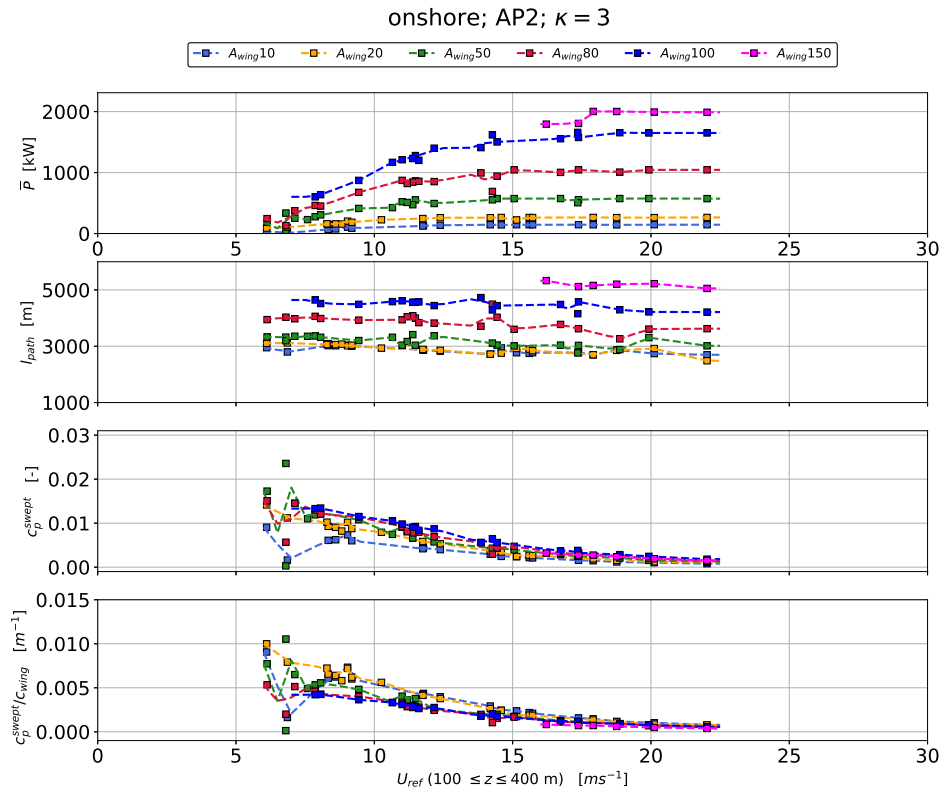


Figure A2. blank

## 700 References

- Ipopt (Interior Point OPTimizer), <https://projects.coin-or.org/Ipopt>, 2016.
- Ampyx: Ampyx Power BV, <https://www.ampyxpower.com/>, 2020.
- Andersson, J., VAAkesson, J., and Diehl, M.: CasADi: A Symbolic Package for Automatic Differentiation and Optimal Control, in: Recent Advances in Algorithmic Differentiation, edited by Forth, S., Hovland, P., Phipps, E., Utke, J., and Walther, A., pp. 297–307, Springer Berlin Heidelberg, Berlin, Heidelberg, 2012.
- Argatov, I. and Silvennoinen, R.: Efficiency of Traction Power Conversion Based on Crosswind Motion, pp. 65–79, Springer Berlin Heidelberg, Berlin, Heidelberg, [https://doi.org/10.1007/978-3-642-39965-7\\_4](https://doi.org/10.1007/978-3-642-39965-7_4), [https://doi.org/10.1007/978-3-642-39965-7\\_4](https://doi.org/10.1007/978-3-642-39965-7_4), 2013.
- awebox: awebox: Modelling and optimal control of single- and multiple-kite systems for airborne wind energy, <https://github.com/awebox>, 2020.
- 710 Bronnenmeyer, T.: Optimal Control for Multi-Kite Emergency Trajectories, Master’s thesis, University of Stuttgart, <https://cdn.syscop.de/publications/Bronnenmeyer2018.pdf>, 2018.
- CasADi: CasADi, <https://github.com/casadi/casadi>, 2016.
- Champion, K. S. W., Cole, A. E., and Kantor, A. J.: Chapter 14 Standard and Reference Atmospheres, 1985.
- De Schutter, J., Leuthold, R., Bronnenmeyer, T., Paelinck, R., and Diehl, M.: Optimal control of stacked multi-kite systems for utility-scale  
715 airborne wind energy, in: 2019 IEEE 58th Conference on Decision and Control (CDC), pp. 4865–4870, 2019.
- Diehl, M.: Airborne Wind Energy: Basic Concepts and Physical Foundations, in: Airborne Wind Energy, edited by Ahrens, U., Diehl, M., and Schmehl, R., pp. 3–22, Springer Berlin Heidelberg, Berlin, Heidelberg, [https://doi.org/10.1007/978-3-642-39965-7\\_1](https://doi.org/10.1007/978-3-642-39965-7_1), [https://doi.org/10.1007/978-3-642-39965-7\\_1](https://doi.org/10.1007/978-3-642-39965-7_1), 2013.



**Figure A3.** power curves onshore AP2

Dörenkämper, M., Olsen, B. T., Witha, B., Hahmann, A. N., Davis, N. N., Barcons, J., Ezber, Y., García-Bustamante, E., González-Rouco, J. F., Navarro, J., Sastre-Marugán, M., Sīle, T., Trei, W., Žagar, M., Badger, J., Gottschall, J., Sanz Rodrigo, J., and Mann, J.: The Making of the New European Wind Atlas – Part 2: Production and Evaluation, *Geosci. Model Dev. Discuss.*, 2020, 1–37, <https://doi.org/10.5194/gmd-2020-23>, 2020.

Drela, M. and Youngren, H.: AVL, <http://web.mit.edu/drela/Public/web/avl/>, 2016.

Echeverri, P., Fricke, T., Homsy, G., and Tucker, N.: The Energy Kite - Selected Results From the Design, Development and Testing of Makani's Airborne Wind Turbines - Part 1, Technical Report 1, Makani Power, [https://storage.googleapis.com/x-prod.appspot.com/files/Makani\\_TheEnergyKiteReport\\_Part1.pdf](https://storage.googleapis.com/x-prod.appspot.com/files/Makani_TheEnergyKiteReport_Part1.pdf), 2020.

Eijkelhof, D., Rapp, S., Fasel, U., Gaunaa, M., and Schmehl, R.: Reference Design and Simulation Framework of a Multi-Megawatt Airborne Wind Energy System, *Journal of Physics: Conference Series*, 1618, 032 020, <https://doi.org/10.1088/1742-6596/1618/3/032020>, <https://doi.org/10.1088/1742-6596/1618/3/032020>, 2020.

Ellis, G. and Ferraro, G.: The Social Acceptance of Wind Energy: Where we stand and the path ahead., Eur - scientific and technical research reports, European Commission, <https://doi.org/10.2789/696070>, 2016.

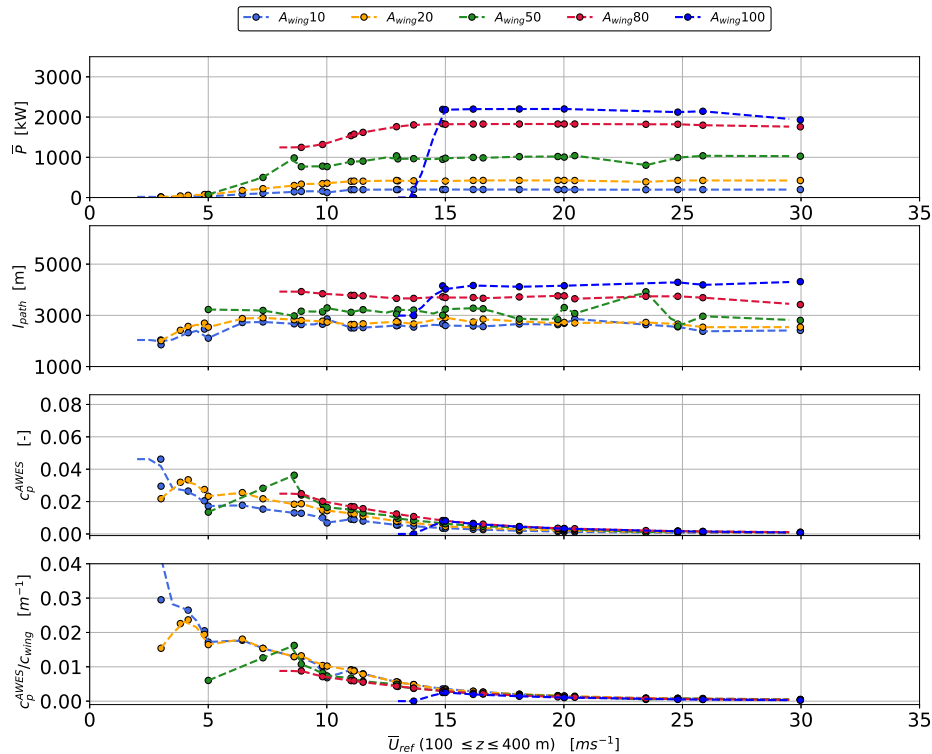


**Figure A4.** power curves onshore AP2-

Federal Aviation Agency: Part 23 - AIRWORTHINESS STANDARDS: NORMAL, UTILITY, ACROBATIC, AND COMMUTER CATEGORY AIRPLANES,

<https://www.govinfo.gov/content/pkg/CFR-2017-title14-vol1/xml/CFR-2017-title14-vol1-part23.xml#seqnum23.337>, 2017.

735 Fingersh, L., Hand, M., and Laxson, A.: Wind Turbine Design Cost and Scaling Model, Tech. rep., <https://doi.org/10.2172/897434>, 2006.

Gros, S., Zanon, M., and Diehl, M.: A relaxation strategy for the optimization of airborne wind energy systems, in: Control Conference (ECC), 2013 European, pp. 1011–1016, IEEE, [http://ieeexplore.ieee.org/xpls/abs\\_all.jsp?arnumber=6669670](http://ieeexplore.ieee.org/xpls/abs_all.jsp?arnumber=6669670), 2013.

Haas, T., De Schutter, J., Diehl, M., and Meyers, J.: Wake characteristics of pumping mode airborne wind energy systems, in: Journal of Physics: Conference Series, vol. 1256, p. 012016, IOP Publishing, 2019.

740 Horn, G., Gros, S., and Diehl, M.: Numerical trajectory optimization for airborne wind energy systems described by high fidelity aircraft models, in: Airborne wind energy, pp. 205–218, Springer, [http://link.springer.com/chapter/10.1007/978-3-642-39965-7\\_11](http://link.springer.com/chapter/10.1007/978-3-642-39965-7_11), 2013.

Houska, B. and Diehl, M.: Optimal control for power generating kites, in: Control Conference (ECC), 2007 European, pp. 3560–3567, IEEE, [http://ieeexplore.ieee.org/xpls/abs\\_all.jsp?arnumber=7068861](http://ieeexplore.ieee.org/xpls/abs_all.jsp?arnumber=7068861), 2007.

HSL: The HSL Mathematical Software Library @ONLINE, <http://www.hsl.rl.ac.uk/>, 2020.

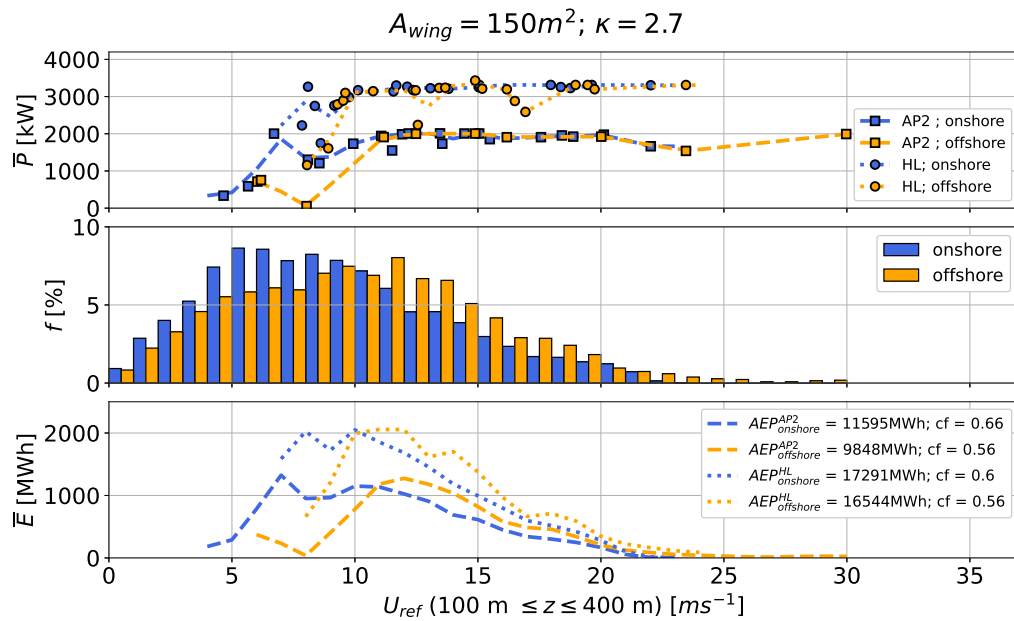


**Figure A5.** ~~power curves onshore AP2~~

- 745 Hurt, H. J.: Aerodynamics for naval aviators, [https://www.faa.gov/regulations\\_policies/handbooks\\_manuals/aviation/media/00-80t-80.pdf](https://www.faa.gov/regulations_policies/handbooks_manuals/aviation/media/00-80t-80.pdf), 1965.
- Kermode, A., Barnard, R., and Philpott, D.: Mechanics of Flight, Pearson Prentice Hall, <https://books.google.co.jp/books?id=cp7CQgAACAAJ>, 2006.
- Kruijff, M. and Ruiterkamp, R.: A Roadmap Towards Airborne Wind Energy in the Utility Sector, pp. 643–662, Springer Singapore, Singapore, [https://doi.org/10.1007/978-981-10-1947-0\\_26](https://doi.org/10.1007/978-981-10-1947-0_26), [https://doi.org/10.1007/978-981-10-1947-0\\_26](https://doi.org/10.1007/978-981-10-1947-0_26), 2018.
- 750 Lee, T. and Su, Y.: Lift enhancement and flow structure of airfoil with joint trailing-edge flap and Gurney flap, Experiments in Fluids, <https://doi.org/10.1007/s00348-010-1024-8>, 2010.
- Leuthold, R., De Schutter, J., Malz, E., Licitra, G., Gros, S., and Diehl, M.: Operational Regions of a Multi-Kite AWE System, pp. 52–57, <https://doi.org/10.23919/ECC.2018.8550199>, 2018.
- 755 Loyd, M. L.: Crosswind kite power (for large-scale wind power production), Journal of Energy, 4, 106–111, <https://doi.org/10.2514/3.48021>, <https://doi.org/10.2514/3.48021>, 1980.
- Luchsinger, R. H.: Pumping Cycle Kite Power, pp. 47–64, Springer Berlin Heidelberg, Berlin, Heidelberg, [https://doi.org/10.1007/978-3-642-39965-7\\_3](https://doi.org/10.1007/978-3-642-39965-7_3), [https://doi.org/10.1007/978-3-642-39965-7\\_3](https://doi.org/10.1007/978-3-642-39965-7_3), 2013.
- Lunney, E., Ban, M., Duic, N., and Foley, A.: A state-of-the-art review and feasibility analysis of high altitude wind power in Northern  
760 Ireland, Renewable and Sustainable Energy Reviews, 68, 899 – 911, <https://doi.org/https://doi.org/10.1016/j.rser.2016.08.014>, 2017.
- Makani: Makani Technologies LLC, <https://x.company/projects/makani/>, 2020.

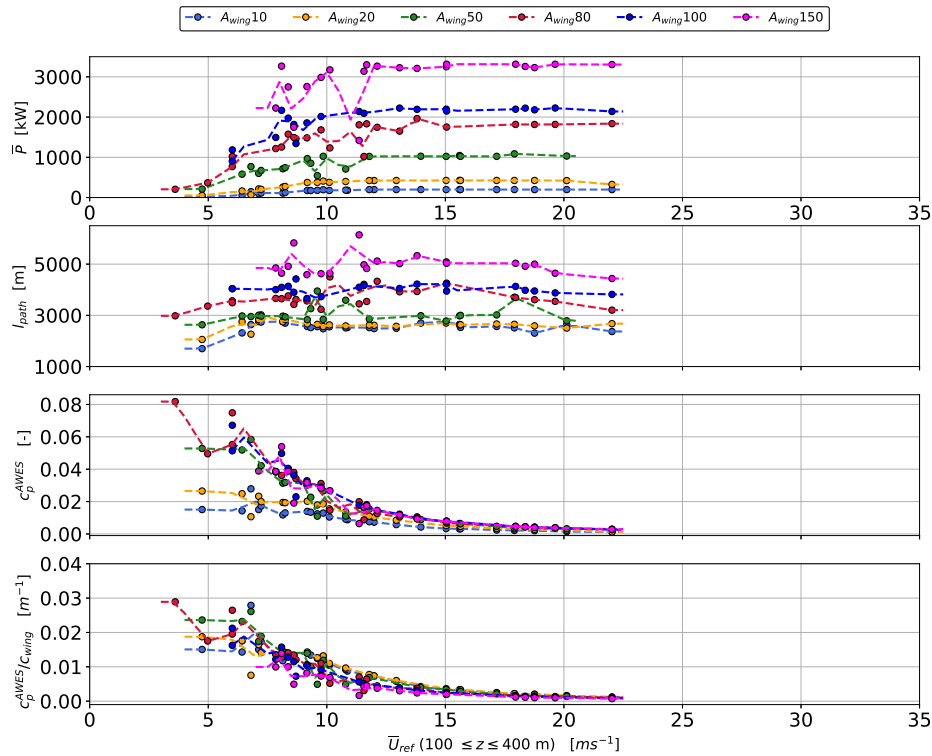


**Figure A6.** power curves onshore HL

- Malz, E., Koenemann, J., Sieberling, S., and Gros, S.: A reference model for airborne wind energy systems for optimization and control, *Renewable Energy*, 140, 1004 – 1011, <https://doi.org/https://doi.org/10.1016/j.renene.2019.03.111>, <http://www.sciencedirect.com/science/article/pii/S0960148119304239>, 2019.
- 765 Malz, E., Verendel, V., and Gros, S.: Computing the power profiles for an Airborne Wind Energy system based on large-scale wind data, *Renewable Energy*, 162, 766 – 778, <https://doi.org/https://doi.org/10.1016/j.renene.2020.06.056>, <http://www.sciencedirect.com/science/article/pii/S0960148120309666>, 2020.
- Malz, E. C., Zanon, M., and Gros, S.: A Quantification of the Performance Loss of Power Averaging in Airborne Wind Energy Farms, in: 2018 European Control Conference (ECC), pp. 58–63, 2018.
- 770 offshorewind.biz: Ampyx Power Taking First Steps Towards MW-Scale Kite, Online, <https://www.offshorewind.biz/2018/12/04/ampyx-power-taking-first-steps-towards-mw-scale-kite/>.
- Pedregosa, F., Varoquaux, G., Gramfort, A., Michel, V., Thirion, B., Grisel, O., Blondel, M., Prettenhofer, P., Weiss, R., Dubourg, V., Vanderplas, J., Passos, A., Cournapeau, D., Brucher, M., Perrot, M., and Duchesnay, E.: Scikit-learn: Machine Learning in Python, *Journal of Machine Learning Research*, 12, 2825–2830, 2011.

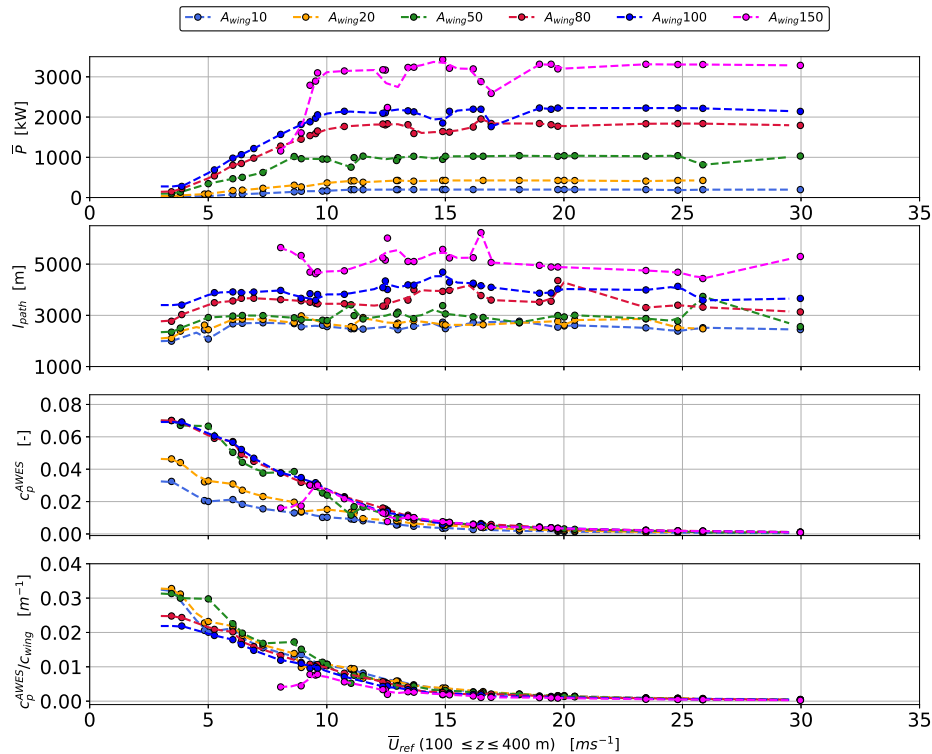


**Figure A7. power curves onshore HL**

- 775 Salvação, N. and Guedes Soares, C.: Wind resource assessment offshore the Atlantic Iberian coast with the WRF model, *Energy*, 145, 276 – 287, <https://doi.org/https://doi.org/10.1016/j.energy.2017.12.101>, <http://www.sciencedirect.com/science/article/pii/S0360544217321448>, 2018.
- Schelbergen, M., Kalverla, P. C., Schmehl, R., and Watson, S. J.: Clustering wind profile shapes to estimate airborne wind energy production, *Wind Energy Science Discussions*, 2020, 1–34, <https://doi.org/10.5194/wes-2019-108>, <https://www.wind-energ-sci-discuss.net/wes-2019-108/>, 2020.
- 780 Schmehl, R., Noom, M., and van der Vlugt, R.: Traction Power Generation with Tethered Wings, in: *Airborne Wind Energy*, chap. 2, pp. 23–45, Springer Berlin Heidelberg, Berlin, Heidelberg, [https://doi.org/10.1007/978-3-642-39965-7\\_2](https://doi.org/10.1007/978-3-642-39965-7_2), 2013.
- Scholz, D.: Aircraft Design - an Open Educational Resource (OER) for Hamburg Open Online University (HOOU), <http://HOOU.ProfScholz.de>, last accessed: 11.10.2021, 2016.
- 785 Sommerfeld, M.: Power curve characterization for ground-generation AWES, *Wind Energy Science*, 2020.
- Sommerfeld, M., Crawford, C., Monahan, A., and Bastigkeit, I.: LiDAR-based characterization of mid-altitude wind conditions for airborne wind energy systems, *Wind Energy*, 0, <https://doi.org/10.1002/we.2343>, 2019a.

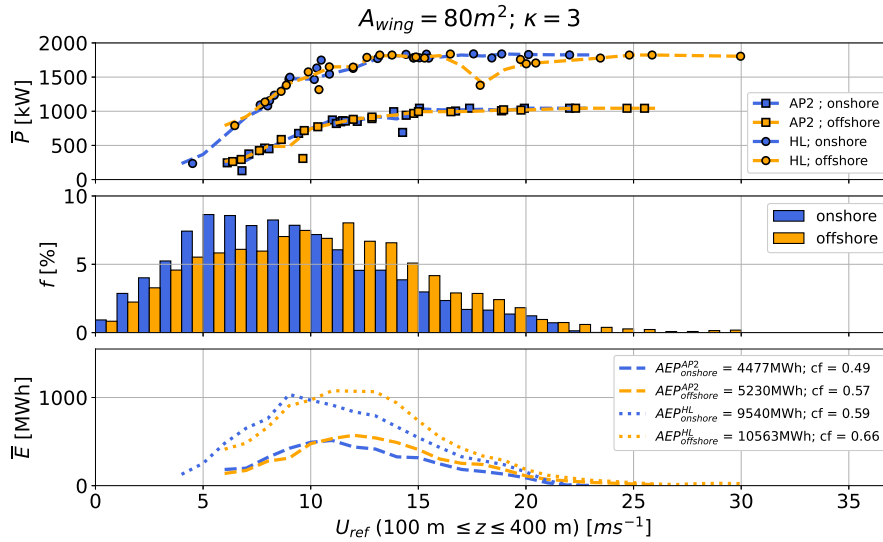


Figure A8. blank

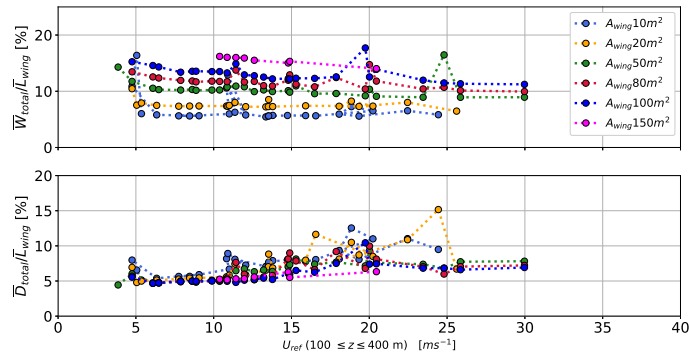


Figure A9. blank

Sommerfeld, M., Dörenkämper, M., Steinfeld, G., and Crawford, C.: Improving mesoscale wind speed forecasts using lidar-based observation nudging for airborne wind energy systems, *Wind Energy Science*, 4, 563–580, <https://doi.org/10.5194/wes-4-563-2019>, <https://www.wind-energy-sci.net/4/563/2019/>, 2019b.

790 Stull, R.: *An Introduction to Boundary Layer Meteorology*, Atmospheric and Oceanographic Sciences Library, Springer Netherlands, <https://books.google.ca/books?id=eRRz9RNvNOKC>, 1988.

Torenbeek, E. and Wittenberg, H.: *Flight Physics: Essentials of Aeronautical Disciplines and Technology, with Historical Notes*, Springer Netherlands, <https://books.google.ca/books?id=VIjEZPyGRIAC>, 2009.

795 van der Vlugt, R., Bley, A., Noom, M., and Schmehl, R.: Quasi-steady model of a pumping kite power system, *Renewable Energy*, 131, 83–99, <https://doi.org/10.1016/j.renene.2018.07.023>, <http://www.sciencedirect.com/science/article/pii/S0960148118308206>, 2019.

Wächter, A. and Biegler, L. T.: On the implementation of an interior-point filter line-search algorithm for large-scale nonlinear programming, *Mathematical Programming*, 106, 25–57, <https://doi.org/10.1007/s10107-004-0559-y>, <https://doi.org/10.1007/s10107-004-0559-y>, 2006.